Tracing the cosmic web

Noam I. Libeskind,[1]* Rien van de Weygaert,[2] Marius Cautun,[3] Bridget Falck,[4]
Elmo Tempel,[1,5] Tom Abel,[6,7] Mehmet Alpaslan,[8] Miguel A. Aragón-Calvo,[9]
Jaime E. Forero-Romero,[10] Roberto Gonzalez,[11,12] Stefan Gottlöber,[1] Oliver Hahn,[13]
Wojciech A. Hellwing,[14,15] Yehuda Hoffman,[16] Bernard J. T. Jones,[2]
Francisco Kitaura,[17,18] Alexander Knebe,[19,20] Serena Manti,[21] Mark Neyrinck,[3]
Sebastián E. Nuza,[1,22] Nelson Padilla,[11,12] Erwin Platen,[2] Nesar Ramachandra,[23]
Aaron Robotham,[24] Enn Saar,[5] Sergei Shandarin,[23] Matthias Steinmetz,[1]
Radu S. Stoica,[25,26] Thierry Sousbie[27] and Gustavo Yepes[18]

Affiliations are listed at the end of the paper

ABSTRACT

The cosmic web is one of the most striking features of the distribution of galaxies and dark matter on the largest scales in the Universe. It is composed of dense regions packed full of galaxies, long filamentary bridges, flattened sheets and vast low-density voids. The study of the cosmic web has focused primarily on the identification of such features, and on understanding the environmental effects on galaxy formation and halo assembly. As such, a variety of different methods have been devised to classify the cosmic web – depending on the data at hand, be it numerical simulations, large sky surveys or other. In this paper, we bring 12 of these methods together and apply them to the same data set in order to understand how they compare. In general, these cosmic-web classifiers have been designed with different cosmological goals in mind, and to study different questions. Therefore, one would not a priori expect agreement between different techniques; however, many of these methods do converge on the identification of specific features. In this paper, we study the agreements and disparities of the different methods. For example, each method finds that knots inhabit higher density regions than filaments, etc. and that voids have the lowest densities. For a given web environment, we find a substantial overlap in the density range assigned by each web classification scheme. We also compare classifications on a halo-by-halo basis; for example, we find that 9 of 12 methods classify around a third of group-mass haloes (i.e. $M_{\rm halo} \sim 10^{13.5}\,h^{-1}\,{\rm M_\odot}$) as being in filaments. Lastly, so that any future cosmic-web classification scheme can be compared to the 12 methods used here, we have made all the data used in this paper public.

Key words: methods: data analysis – dark matter – large-scale structure of the Universe – cosmology: theory.

1 INTRODUCTION

On megaparsec scales the matter and galaxy distribution is not uniform, but defines an intricate multiscale interconnected network that is known as the *cosmic web* (Bond, Kofman & Pogosyan 1996). It represents the fundamental spatial organization of matter on scales of a few up to a hundred megaparsec. Galaxies, intergalactic gas and dark matter arrange themselves in a salient wispy pattern of dense compact clusters, long elongated filaments and sheet-like tenuous walls surrounding near-empty void regions. Ubiquitous throughout the entire observable Universe, such patterns exist at nearly all epochs, albeit at smaller scales. It defines a complex spatial pattern of intricately connected structures, displaying a rich geometry with multiple morphologies and shapes. This complexity is considerably enhanced by its intrinsic multiscale nature, including objects over

*E-mail: nlibeskind@aip.de

a considerable range of spatial scales and densities. For, a recent up-to-date report on a wide range of relevant aspects of the cosmic web, we refer to the volume by van de Weygaert et al. (2016).

The presence of the web-like pattern can be easily seen in the spatial distribution of galaxies. Its existence was suggested by early attempts to map the nearby cosmos in galaxy redshift surveys (Gregory, Thompson & Tifft 1978; Jõeveer, Einasto & Tago 1978; de Lapparent, Geller & Huchra 1986; Geller & Huchra 1989; Shectman et al. 1996). Particularly, iconic was the publication of the *slice of the Universe* by de Lapparent et al. (1986). Since then, the impression of a web-like arrangement of galaxies has been confirmed many times by large galaxy redshift surveys such as 2dFGRS (Colless et al. 2003; van de Weygaert & Schaap 2009), the Sloan Digital Sky Survey (SDSS; Tegmark et al. 2004) and the 2MASS redshift survey (Huchra et al. 2012), as well as by recently produced maps of the galaxy distribution at larger cosmic depths such as VIPERS (Guzzo et al. 2014). From cosmological *N*-body simulations (e.g. Springel et al. 2005; Vogelsberger et al. 2014; Schaye et al. 2015) and recent Bayesian reconstructions of the underlying dark matter distribution in the local Universe (Heß, Kitaura & Gottlöber 2013; Kitaura 2013; Nuza et al. 2014; Leclercq, Jasche & Wandelt 2015b; Sorce et al. 2016), we have come to realize that the web-like pattern is even more pronounced and intricate in the distribution of dark matter.

1.1 The components of the cosmic web

The most prominent and defining features of the cosmic web are the filaments. The most outstanding specimen in the local Universe is the Pisces–Perseus chain (Giovanelli & Haynes 1985). A recent systematic inventory of filaments in the SDSS galaxy redshift distribution has been catalogued by (Tempel et al. 2014, also see Jones, van de Weygaert & Aragón-Calvo 2010; Sousbie, Pichon & Kawahara 2011). Filaments appear to be the highways of the Universe, the transport channels along which mass and galaxies get channelled into the higher density cluster regions (van Haarlem & van de Weygaert 1993; Knebe et al. 2004) and which define the connecting structures between higher density complexes (Bond et al. 1996; Colberg, Krughoff & Connolly 2005; van de Weygaert & Bond 2008; Aragón-Calvo, van de Weygaert & Jones 2010b). On the largest scales, filaments on scales of 10 up to 100 Mpc are found to connect complexes of superclusters – such as the great attractor (Lynden-Bell et al. 1988), the Shapley concentration (Shapley 1930; Proust et al. 2006) or more recently the Vela supercluster (Kraan-Korteweg et al. 2017) – as was, for example, indicated by the work of Bharadwaj, Bhavsar & Sheth (2004), Romano-Díaz & van de Weygaert (2007) and Libeskind et al. (2015a).

By contrast, the tenuous sheet-like membranes are considerably more difficult to find in the spatial mass distribution traced by galaxies. Their low surface density renders them far less conspicuous than the surrounding filaments, while they are populated by galaxies with a considerably lower luminosity (see e.g. Cautun et al. 2014). When looking at the spatial structure outlined by clusters, we do recognize more prominent flattened supercluster configurations, often identified as *Great Walls*, which is a reflection of their dynamical youth. Particularly outstanding specimens are the CfA Great Wall (Geller & Huchra 1989), the Sloan Great Wall (Gott et al. 2005) and most recently the BOSS Great Wall (Lietzen et al. 2016) and the well-established supergalactic plane (de Vaucouleurs 1953; Lahav et al. 2000).

Along with filaments, the large void regions represent the most prominent aspect of the megaparsec scale Universe. These are enormous regions with sizes in the range of 20–50 h^{-1} Mpc which are practically devoid of any galaxy, usually roundish in shape and occupying the major share of space in the Universe (see van de Weygaert 2016, for a recent review). Forming an essential and prominent aspect of the *cosmic web* (Bond et al. 1996), voids are instrumental in the spatial organization of the cosmic web (Icke 1984; Sahni, Sathyaprakash & Shandarin 1994; Sheth & van de Weygaert 2004; Einasto et al. 2011; Aragon-Calvo & Szalay 2013). The first indication for their existence was found in early galaxy redshift samples (Chincarini & Rood 1975; Gregory, Thompson & Tifft 1978; Zeldovich, Einasto & Shandarin 1982), while the discovery of the 50 Mpc size Boötes void by Kirshner et al. (1981), Kirshner et al. (1987) and the CfA study by de Lapparent et al. (1986) established them as key aspects of the large-scale galaxy distribution. Recent studies have been mapping and cataloguing the void population in the local Universe (Fairall 1998; Pan et al. 2012; Sutter et al. 2012), and even that in the implied dark matter distribution (Leclercq et al. 2015a). In the immediate vicinity of our Milky Way, one of the most interesting features is in fact the Local Void whose diameter is around 30 Mpc (Tully & Fisher 1987). Its effectively repulsive dynamical influence has been demonstrated in studies of cosmic flows in the local volume (Tully et al. 2008), while a recent study even indicated the dominant impact of a major depression at a distance of more than 100 Mpc (the so-called dipole repeller; Hoffman et al. 2017).

1.2 Physics and dynamics of the cosmic web

The cosmic web is a direct result of two physical drivers that are at the heart of the current paradigm of structure formation. The first is that the initial density field is a Gaussian random field, described by a power spectrum of density fluctuations (Adler 1981; Bardeen et al. 1986). The second is that these perturbations evolve entirely due to gravity (Peebles 1980). Gravitational instability is responsible for increasing the contrast in the universe, as rich overdense regions grow in mass and density while shrinking in physical size, and as empty voids expand and come to dominate the volume of the universe. Once the gravitational clustering process begins to go beyond the linear growth phase, we see the emergence of complex patterns and structures in the density field.

Within the gravitationally driven emergence and evolution of cosmic structure, the web-like patterns in the overall cosmic matter distribution do represent a universal but possibly transient phase. As borne out by a large array of *N*-body computer experiments of cosmic structure formation (e.g. Springel et al. 2005; Vogelsberger et al. 2014; Dubois et al. 2014; Schaye et al. 2015), web-like patterns defined by prominent anisotropic filamentary and planar features – and with characteristic large underdense void regions – are the natural outcome of the gravitational cosmic structure formation process. They are the manifestation of the anisotropic nature of gravitational collapse, and mark the transition from the primordial (Gaussian) random field to highly non-linear structures that have fully collapsed into haloes and galaxies. Within this context, the formation and evolution of anisotropic structures are the product of anisotropic deformations accurately described by the Zel'dovich formalism in the mildly non-linear stage, driven by gravitational tidal forces induced by the inhomogeneous mass distribution. In other words, it is the anisotropy of the force field and the resulting deformation of the matter distribution which are at the heart of the emergence of the web-like structure of the mildly non-linear mass

distribution (also see Bond et al. 1996; Hahn et al. 2007a; van de Weygaert & Bond 2008; Forero-Romero et al. 2009).

This idea was first pointed out by Zel'dovich (1970, also see Icke 1973) who described, in the now seminal '*Zel'dovich approximation*' framework, how gravitational collapse amplifies any initial anisotropies and gives rise to highly anisotropic structures. Accordingly, the final morphology of a structure depends on the eigenvalues of the deformation tensor. Sheets, filaments and clusters correspond to domains with one, two and three positive eigenvalues, while voids correspond to regions with all negative eigenvalues. Based on this realization, Doroshkevich (1970) derived a range of analytical predictions for structure emerging from an initial field of Gaussian perturbations. In the emerging picture of structure formation, also known as Zel'dovich's pancake picture, anisotropic collapse has a well-defined sequence, with regions first contracting along one axis to form sheets, then along the second axis to produce filaments and only at the end to fully collapse along each direction (Shandarin & Zel'dovich 1989; Shandarin & Sunyaev 2009).

Following up on this, the early evolution of the cosmic web can be understood in detail in terms of the singularities and caustics that are arising in the matter distribution as a result of the structure of the corresponding flow field (see Shandarin & Zel'dovich 1989; Hidding, Shandarin & van de Weygaert 2014). Indeed, one of the most interesting recent developments in our understanding of the dynamical evolution of the cosmic web has been the uncovering of the intimate link between the emerging anisotropic structures and the multistream migration flows involved in the buildup of cosmic structure (Shandarin 2011; Abel, Hahn & Kaehler 2012; Falck, Neyrinck & Szalay 2012; Neyrinck 2012; Shandarin, Habib & Heitmann 2012).

Also recent observational advances have enabled new profound insights into the dynamical processes that are shaping the cosmic web in our local Universe. In particular, the Cosmicflows-2 and Cosmicflows-3 surveys of galaxy peculiar velocities in our local Universe have produced tantalizing results (Courtois et al. 2013; Tully et al. 2014), opening up a window on the flows of mass along and towards structures in the local cosmic web. Amongst others, these studies show the sizeable impact of low-density void regions on the dynamics in the vicinity of the Milky Way and have allowed the velocity shear based V-web identification of web-like components in the local Universe (Libeskind et al. 2015a; Pomarède et al. 2015; Hoffman et al. 2017).

The extension of the Zel'dovich approximation, the *adhesion approximation*, allows further insights into the hierarchical buildup of the cosmic web (Gurbatov, Saichev & Shandarin 1989; Kofman, Pogosian & Shandarin 1990; Kofman et al. 1992; Hidding et al. 2012). By introducing an artificial viscosity term, the adhesion approximation mitigates some of the late-time limitations of the Zel'dovich approximation. It also leads to a profound understanding of the link between the evolving phase-space structure of the cosmic matter distribution and the tendency to continuously morph the emerging spatial structure into one marked by ever larger structures (see also Sahni & Coles 1995, for a review of analytical extensions to the Zel'dovich approximation).

Interestingly, for a considerable amount of time the emphasis on anisotropic collapse as agent for forming and shaping structure in the Zel'dovich pancake picture was seen as the rival view to the purely hierarchical clustering picture. In fact, the successful synthesis of both elements culminated in the *cosmic -web* theory (Bond et al. 1996), which stresses the dominance of filamentary shaped features and appears to provide a successful description of large-scale structure formation in the ΛCDM cosmology. This theoretical framework pointed out the dynamical relationship between the filamentary patterns and the compact dense clusters that stand out as the nodes within the cosmic matter distribution: filaments as cluster–cluster bridges (also see Bond et al. 1996; van de Weygaert & Bertschinger 1996; Colberg et al. 2005; van de Weygaert & Bond 2008). In the overall cosmic mass distribution, clusters – and the density peaks in the primordial density field that are their precursors – stand out as the dominant features for determining and outlining the anisotropic force field that generates the cosmic web. The cosmic-web theory embeds the anisotropic evolution of structures in the cosmic web within the context of the hierarchically evolving mass distribution (Bond & Myers 1996). Meanwhile, complementary analytical descriptions of a hierarchically evolving cosmic web within the context of excursion set theory form the basis for a statistical evaluation of its properties (Sheth & van de Weygaert 2004; Shen et al. 2006).

1.3 Significance and impact of the cosmic web

Understanding the nature of the cosmic web is important for a variety of reasons. Quantitative measures of the cosmic web may provide information about the dynamics of gravitational structure formation, the background cosmological model, the nature of dark matter and ultimately the formation and evolution of galaxies. Since the cosmic web defines the fundamental spatial organization of matter and galaxies on scales of one to tens of megaparsecs, its structure probes a wide variety of scales, form the linear to the non-linear regime. This suggests that quantification of the cosmic web at these scales should provide a significant amount of information regarding the structure formation process. As yet, we are only at the beginning of systematically exploring the various structural aspects of the cosmic web and its components towards gaining deeper insights into the emergence of spatial complexity in the Universe (see e.g. Cautun et al. 2014).

The cosmic web is also a rich source of information regarding the underlying cosmological model. The evolution, structure and dynamics of the cosmic web are to a large extent dependent on the nature of dark matter and dark energy. As the evolution of the cosmic web is directly dependent on the rules of gravity, each of the relevant cosmological variables will leave its imprint on the structure, geometry and topology of the cosmic web and the relative importance of the structural elements of the web, i.e. of filaments, walls, cluster nodes and voids. A telling illustration of this is the fact that void regions of the cosmic web offer one of the cleanest probes and measures of dark energy as well as tests of gravity and general relativity. Their structure and shape, as well as mutual alignment, are direct reflections of dark energy (Park & Lee 2007; Platen, van de Weygaert & Jones 2008; Lee & Park 2009; Lavaux & Wandelt 2010, 2012; Bos et al. 2012; Pisani et al. 2015; Sutter et al. 2015). Given that the measurement of cosmological parameters depends on the observer's web environment (e.g. Wojtak et al. 2014), one of our main objectives is to develop means of exploiting our measures of filament structure and dynamics, and the connectivity characteristics of the web-like network, towards extracting such cosmological information.

Perhaps the most prominent interest in developing more objective and quantitative measures of large-scale cosmic-web environments concerns the environmental influence on the formation and evolution of galaxies, and the dark matter haloes in which they form (see e.g. Hahn et al. 2007b; Hahn 2009; Cautun et al. 2014). The canonical example of such an influence is that of the origin of the rotation of galaxies: the same tidal forces responsible for the torquing of

collapsing protogalactic haloes (Hoyle 1951; Peebles 1969; Doroshkevich 1970) are also directing the anisotropic contraction of matter in the surroundings. We may therefore expect to find an alignment between galaxy orientations and large-scale filamentary structure, which indeed currently is an active subject of investigation (e.g. Aragón-Calvo et al. 2007b; Lee & Pen 2000; Jones, van de Weygaert & Aragón-Calvo 2010; Codis et al. 2012; Libeskind et al. 2013a; Tempel & Libeskind 2013; Tempel, Stoica & Saar 2013; Trowland 2013; Trowland, Lewis & Bland-Hawthorn 2013; Aragón-Calvo & Yang 2014; Pahwa et al. 2016; González et al. 2017; Hirv et al. 2017). Some studies even claim that this implies an instrumental role of filamentary and other web-like environments in determining the morphology of galaxies (see e.g. Pichon et al. 2016, for a short review). Indeed, the direct impact of the structure and connectivity of filamentary web on the star formation activity of forming galaxies has been convincingly demonstrated by Dekel et al. (2009a, see also Dekel, Sari & Ceverino 2009b; Danovich et al. 2015; Goerdt et al. 2015; Aragón-Calvo, Neyrinck & Silk 2016). Such studies point out the instrumental importance of the filaments as transport conduits of cold gas on to the forming galaxies, and hence the implications of the topology of the network in determining the evolution and final nature. Such claims are supported by a range of observational findings, of which the morphology–density relation (Dressler 1980) is best known as relating intrinsic galaxy properties with the cosmic environment in which the galaxies are embedded (see e.g. Kuutma, Tamm & Tempel 2017). A final example of a possible influence of the cosmic web on the nature of galaxies concerns a more recent finding that has led to a vigorous activity in seeking to understand it. The satellite galaxy systems around the Galaxy and M31 have been found to be flattened. It might be that their orientation points at a direct influence of the surrounding large-scale structures (see Ibata et al. 2013; Cautun et al. 2015; Forero-Romero & González 2015; Gillet et al. 2015; Libeskind et al. 2015a; González & Padilla 2016), for example a reflection of local filament or local sheet.

1.4 Detection and classification of cosmic-web structure

To enable further advances in the astronomical issues addressed above, we need to establish a more objective description and quantification of the structure seen in the cosmic web. However, extracting such topological and morphological information from a discrete set of points, provided by either an *N*-body simulation or a galaxy survey, is very difficult. As such, many different methods have been developed to tackle this problem (reviewed in depth in Section 4). Some of the problems faced by observational surveys include sampling errors, projection effects, observational errors, incomplete sky coverage, magnitude limits, as well as various biases (e.g. Malmquist bias, selection bias). On the other hand, *N*-body simulations return the full 6D phase space and density field of the simulated universe at any desired epoch. A method that takes full advantage of this often unobservable information cannot be directly applied to observations, but can be applied to simulations constrained to match observations (e.g. Leclercq et al. 2017). For this reason, methods that are developed specifically for the analysis of numerical simulations, may be completely inapplicable to current observational data sets and vice versa. Yet the numerous articles in the literature which attempt to study the cosmic web often refer to the same structural hierarchy: knots, filaments, sheets and voids. Here, we use a numerical simulation to compare classifiers that, regardless of their position on the theoretical to observational

spectrum, speak the same language of knots, filaments, sheets and voids.

In the spirit of previous structure finder comparison projects (Colberg et al. 2008; Knebe et al. 2011, etc.), we present a comparison of cosmic-web identification codes and philosophies. However, our comparison differs significantly from e.g. the seminal Santa Barbara comparison project (Frenk et al. 1999) or other tests of codes which purport to model the same physical process (e.g. Scannapieco et al. 2012; Knebe et al. 2013). Instead, the methods compared here were developed for very different purposes, to be applied to different kinds of data and with different goals in mind. Some of the methods are based on treating galaxies (haloes) as points; while others were developed to be applied to density or velocity fields. Furthermore, unlike halo finders seeking collapsed or bound objects, there is no robust analytical theory (such as the spherical top hat collapse model of Sheth & Tormen 1999) which we may use as a guide for how we expect different cosmic-web finders to behave. Therefore, we enter into this comparison fully expecting large disagreements between the methods examined.

1.5 Outline

This paper is laid out as follows: in Section 2, we group the different methods into 'families' that follow broadly similar approaches. In Section 3, we present the test data set that has been used as the basis for our comparison. In Section 4, we review each method that has taken part in the comparison. In Section 5, we describe the results of the comparison. In Section 6, we summarize our results and draw conclusions.

2 WEB IDENTIFICATION METHODS: CLASSIFICATION

It is a major challenge to characterize the structure, geometry and connectivity of the cosmic web. The complex spatial pattern – marked by a rich geometry with multiple morphologies and shapes, an intricate connectivity, a lack of symmetries, an intrinsic multi-scale nature and a wide range of densities – eludes a sufficiently relevant and descriptive analysis by conventional statistics to quantify the arrangement of mass and galaxies.

Many attempts to analyse the clustering of mass and galaxies at megaparsec scales have been rather limited in their ability to describe and quantify, let alone identify, the features and components of the cosmic web. Measures like the two-point correlation function, which has been the mainstay of many cosmological studies over the past nearly 40 yr (Peebles 1980), are not sensitive to the spatial complexity of patterns in the mass and galaxy distribution. This paper seeks to compare the diverse range of more sophisticated techniques that have been developed over the past few years to address the spatially complex megaparsec scale patterns delineated by mass and galaxies in the Universe.

In the present study, we compare the results and web evaluations and identifications of 12 different formalisms. They are diverse, involving different definitions for the physical identity of the structural features, as well as employing different means of turning these definitions into practical identification tools. The various different methods that have been developed can largely be grouped into five main classes:

(1) *Graph and percolation techniques*. The connectedness of elongated supercluster structures in the cosmic matter distribution was first probed by means of percolation analysis, introduced and

emphasized by Zel'dovich and co-workers (Zeldovich et al. 1982; Shandarin & Zel'dovich 1989; Shandarin, Sheth & Sahni 2004). A related graph-theoretical construct, the minimum spanning tree (MST) of the galaxy distribution, was extensively analysed by Bhavsar and collaborators (Barrow, Bhavsar & Sonoda 1985; Graham & Clowes 1995; Colberg 2007) in an attempt to develop an objective measure of filamentarity. Colberg (2007) set out to identify filaments and their adjoining clusters, using an elaborate set of criteria for the identification of features based on the branching of MSTs. In our study, we involve the MST-based algorithm developed by Alpaslan et al. (2014b) for identification of filaments and void regions in the GAMA survey (Alpaslan et al. 2014a).

(2) *Stochastic methods*. This class of methods involves the statistical evaluation of stochastic geometric concepts. Examples are filament detection algorithms based on the Bayesian sampling of well-defined and parametrized stochastic spatial (marked) point processes that model particular geometric configurations. Stoica, Gregori & Mateu (2005), Stoica, Martínez & Saar (2007), Stoica, Martínez & Saar (2010) and Tempel et al. (2016) use the Bisous model as an object point process of connected and aligned cylinders to locate and catalogue filaments in galaxy surveys. One of the advantages of this approach is that it can be applied directly on the original galaxy point field, given by the positions of the galaxies centres, without requiring the computation of a continuous density field. These methods are computationally very demanding. A thorough mathematical non-parametric formalism involving the medial axis of a point cloud, as yet for 2D point distributions, was proposed by Genovese et al. (2010). It is based on a geometric representation of filaments as the medial axis of the data distribution. Also solidly rooted within a geometric and mathematical context is the more generic geometric inference formalism developed by Chazal, Cohen-Steiner & Mérigot (2009). It allows the recovery of geometric and topological features of the supposedly underlying density field from a sampled point cloud on the basis of distance functions. In addition, we also see the proliferation of tessellation-based algorithms. Following specific physical criteria, González & Padilla (2010) put forward a promising combination of a tessellation-based density estimator and a dynamical binding energy criterion (also see van de Weygaert & Schaap 2009). We may also include another recent development in this broad class of methods. Leclercq et al. (2015b), Leclercq, Jasche & Wandelt (2015c) describe a highly interesting framework for the classification of geometric segments using information theory. Leclercq et al. (2016) have previously compared a few cosmic-web classifiers to each other, judging them on the basis of their information content.

(3a) *Geometric, Hessian-based methods*. A large class of approaches exploits the morphological and (local) geometric information included in the Hessian of the density, tidal or velocity shear fields (e.g. Aragón-Calvo et al. 2007a; Hahn et al. 2007a; Forero-Romero et al. 2009; Bond, Strauss & Cen 2010a; Libeskind et al. 2012; Cautun, van de Weygaert & Jones 2013). Based on the realization that the formation and dynamical evolution of the cosmic web is tied to the tidal force field (see Bond et al. 1996), Hahn et al. (2007a) developed an elaborate classification scheme based on the signature of the tidal tensor (also see Hahn et al. 2007b). A further extension and elaboration of this tidal field based scheme was developed by Forero-Romero et al. (2009), while also the multiscale Nexus formalism incorporates versions that classify web-like features on the tidal tensor signature (Cautun et al. 2013, see below) Following a similar rationale and focusing on the link between emerging web-like structures and the nature of the velocity flow in and around these features, in a sense following up on the classic

realization of such a connection by Zel'dovich (1970), Libeskind, Hoffman and collaborators forwarded the V-web technique (Hoffman et al. 2012; Libeskind et al. 2012, 2013a,b, 2014a,2015a,b; Libeskind, Hoffman & Gottlöber 2014a; Metuki et al. 2015; Carlesi et al. 2016; Metuki, Libeskind & Hoffman 2016; Pahwa et al. 2016). Its classification is explicitly based on the signature of the velocity shear field.

Instead of using the tidal or velocity sheer field configuration, one may also try to link directly to the morphology of the density field itself (Aragón-Calvo et al. 2007a; Bond et al. 2010a; Cautun et al. 2013). Though this allows a more detailed view of the multiscale matter distribution, it is usually more sensitive to noise and less directly coupled to the underlying dynamics of structure formation than the tidal field morphology. A single scale dissection of the density field into its various morphological components has been defined by Bond et al. (2010a), and applied to *N*-body simulations and galaxy redshift samples (also see Bond et al. 2010a; Bond, Strauss & Cen 2010b; Choi et al. 2010).

(3b) *Scale-space multiscale Hessian-based methods*. While most of the Hessian-based formalisms are defined on one particular (smoothing) scale for the field involved, explicit multiscale versions have also been developed. The Multiscale Morphology Filter (MMF)/Nexus MMF formalism of Aragón-Calvo et al. (2007a) and Cautun et al. (2013) look at structure from a *scale-space* point of view, where the (usually Gaussian) smoothing scale of the field defines an extra dimension. This formalism takes into account the multiscale character of the cosmic mass distribution by assessing at each spatial location the prominence of structural signatures, set by the signature of the Hessian of the field involved (Aragón-Calvo et al. 2007a; Cautun et al. 2013). A somewhat similar multiscale approach was followed by the Metric Space Technique described by Wu, Batuski & Khalil (2009), who applied it to a morphological analysis of SDSS-DR5. While the original MMF method (Aragón-Calvo et al. 2007a) involved only the density field, the Nexus formalism extended this to a versatile algorithm that classifies the cosmic web on the basis of a multiscale filter bank applied to either the density, tidal, velocity divergence or velocity shear fields. Applying the technique to the logarithm of the density increases its sensitivity and dynamical range and allows the approach to attain its optimal form, the so-called NEXUS+ method, revealing both major filamentary arteries as well as tiny branching tendrils (Cautun et al. 2013).

(4) *Topological methods*. While the Hessian-based methods concentrate on criteria of the local geometric structure of density, velocity or tidal field, another family of techniques seeks to assess the cosmic web by studying the connectivity and topological properties of the field involved. A typical example involves the delineation of underdense void basins in the large-scale mass distribution by means of the *watershed transform*, in the form of the watershed void finder (Platen, van de Weygaert & Jones 2007) and ZOBOV (Neyrinck 2008). The Spineweb procedure (Aragón-Calvo et al. 2010b) extends this to an elaborate scheme for tracing the various web-like features – filaments, sheets and voids – on purely topological grounds. Spineweb achieves this by identifying the central axis of filaments and the core plane of walls with the boundaries between the watershed basins of the density field. While the basic Spineweb procedure involves one single scale, the full multiscale Spineweb procedure allows a multiscale topological characterization of the cosmic web (Aragón-Calvo et al. 2010a; Aragon-Calvo & Szalay 2013).

In essence, the Spineweb procedure is a practical implementation of the mathematics of Morse theory (Morse 1934). Morse

theory describes the spatial connectivity of the density field on the basis of its singularity structure, i.e. on the location and identity of the singularities – maxima, minima and saddle points – and their spatial connectivity by means of the characteristic lines defined by the gradient field. Colombi, Pogosyan & Souradeep (2000) first described the role of Morse theory in a cosmological context, which subsequently formed the basis of the *skeleton analysis* by (Novikov, Colombi & Doré 2006, 2D) and (Sousbie et al. 2008a, 3D). This defined an elegant and mathematically rigorous tool for filament identification. In a considerably more versatile elaboration of this, invoking the power of topological persistence to identify topologically significant features, Sousbie (2011) has formulated the sophisticated DISPERSE formalism that facilitates the detection of the full array of structural features in the cosmic mass distribution (also see Sousbie et al. 2011). None the less, most of its applications are directed towards outlining the filaments. A further development along these lines, invoking the information provided by persistence measures, is that advocated by Shivashankar et al. (2016).

(5) *Phase-space methods.* Most closely connected to the dynamics of the cosmic-web formation process are several recently proposed formalisms that look at the phase-space structure of the evolving mass distribution (Abel et al. 2012; Falck et al. 2012; Shandarin et al. 2012). They are based on the realization that – in cosmologies in which the intrinsic velocity dispersion of particles in the primordial universe is small – the evolving spatial mass distribution has the appearance of a 3D sheet folding itself in 6D phase space, a *phase space sheet*. By assessing its structure in full phase space, these formalisms trace the mass streams in the flow field reflecting the emergence of non-linear structures. Noting that the emergence of non-linear structures occurs at locations where different streams of the corresponding flow field cross each other, these phase-space methods provide a dynamically based morphological identification of the emerging structures.

This class of methods contains the ORIGAMI formalism (Falck et al. 2012; Falck & Neyrinck 2015), the phase-space sheet methods of (Shandarin 2011, also see Ramachandra & Shandarin 2015) and Abel et al. (2012), and the Claxon formalism (Hidding 2017). The Claxon approach incorporates the modelling of the non-linear evolution of the cosmic mass distribution by means of the adhesion formalism (Gurbatov et al. 1989; Hidding et al. 2012), in order to identify and classify the singularities – shocks – emerging in the evolving structure. Claxon states that these singularities trace the skeleton of the cosmic web.

3 TEST DATA: SIMULATION AND DATA SET

Each of the participants applied their web identification methods to the same GADGET-2 (Springel 2005) dark matter only *N*-body simulation, with a box size of 200 h^{-1} Mpc and 512^3 particles. The ΛCDM cosmological parameters are taken from Planck (Planck Collaboration XVI 2014): $h = 0.68$, $\Omega_M = 0.31$, $\Omega_\Lambda = 0.69$, $n_s = 0.96$ and $\sigma_8 = 0.82$. Haloes in the simulation are identified using a standard FOF algorithm (Davis et al. 1985), with a linking length of $b = 0.2$ and a minimum of 20 particles per halo. Fig. 1 shows a thin slice through the density field and the halo population of this simulation.

The main output of the methods is the classification of the dark matter density field into one of four web components: knot, filament, wall and void. This classification is performed for either volume elements (e.g. the Hessian methods), dark matter mass elements (e.g. the phase-space methods), or for the haloes (e.g. the point process methods). The exact choice was left to the discretion of the

authors to better reflect the procedure used in the studies employing those methods.

Though the output format of the web identification methods may vary, each participant was asked to provide two data sets: the web identification tag defined on a regular grid with a 2 h^{-1} Mpc cell size (100^3 cells) and the web classification of each FOF halo. Most methods returned both data sets except for some of the point-process methods (MST, FINE), for which assigning an environment tag to each grid cell would not make sense. These return information regarding the filamentary environment of just the FOF haloes.

The simulation is made publicly available[1] for exploitation by interested parties. We have included the $z = 0$ GADGET snapshots, the FOF halo catalogue as well as the output of each cosmic-web method included in this work. Where available, each method's classification is returned on a regular grid. Included in the data set is also the FOF catalogue appended with the classification of each halo for each method. We encourage other methods not included in this paper, to use this data set as a bench mark of the community's current status.

4 WEB IDENTIFICATION METHODS: DESCRIPTION AND DETAILS

The following section describes each method as well as the practical details in the analysis of this data set. See Table 1 for a brief summary.

4.1 Adapted minimal spanning tree (Alpaslan and Robotham)

The adapted minimal spanning tree algorithm (Alpaslan et al. 2014a, see also Barrow et al. 1985; Doroshkevich et al. 2004; Colberg 2007) uses a multiple pass approach to detect large-scale structure, similar to Murphy, Eke & Frenk (2011).

Designed to be run on galaxy survey data, the adapted MST algorithm begins by identifying filamentary networks by using galaxy group centroids as nodes for an initial MST; in doing so, redshift-space distortion effects typically present in such data are successfully removed. The maximal allowable distance b between two group (or halo) centres is selected such that at least 90 per cent of groups or haloes with $M_{halo} \geq 10^{11}$ M$_\odot$ are considered to be in filaments. A large b will cause galaxies in voids to be associated with filaments, and a small b will only identify close pairings of groups to be in filaments and ignore the expansive structures visible in the data.

Following the identification of filaments from group centres, galaxies that are within an orthogonal distance r of filaments are associated with those filaments. Additionally, the topological structure of the MST that forms each filament is analysed, with the principal axis of each filament (the so-called backbone) identified as the longest contiguous path of groups that spans the entirety of the filament, along with tributary 'branches' that link to it. The sizes and shapes of these pathways are used to successfully compare observational results to simulated universes in Alpaslan et al. (2014a). Galaxies associated with each filament are further associated with the branch of the filament they are closest to, allowing for a detailed analysis of galaxy properties as a function of filament morphology (Alpaslan et al. 2015, 2016).

---

[1] All the data used in this paper can be found at the following URL: http://data.aip.de/tracingthecosmicweb/. The database was compiled by Noam I Libeskind (doi:10.17876/data/2017_1).
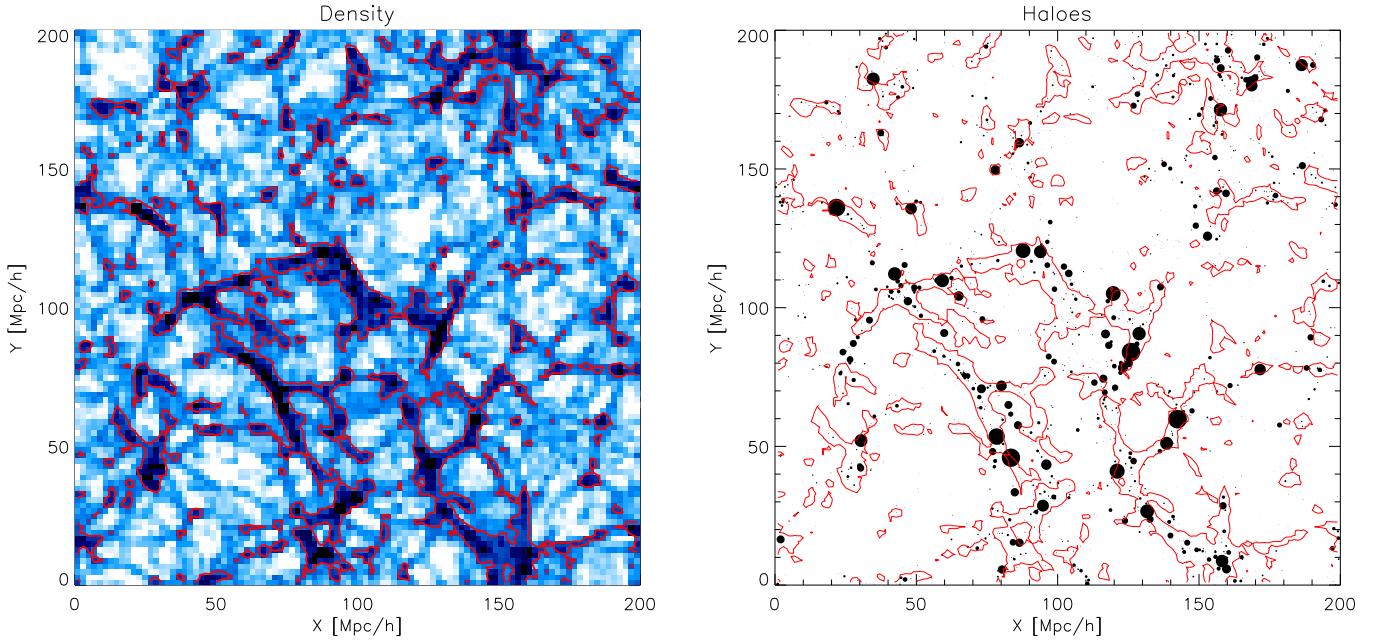
Figure 1. A thin slice through the cosmological simulation used for comparing the web identification methods. The left-hand panel shows the density field in a $2\,h^{-1}$ Mpc slice with darker colours corresponding to higher density regions. The red lines show the $\delta = 0$ contours (dividing overdense and underdense regions, with respect to the mean) and are reproduced in the right-hand panel (and in Fig. 2 as black lines). The right-hand panel shows the positions of haloes in a $10\,h^{-1}$ Mpc slice, where symbol sizes are scaled by halo mass. This same slice will be used to showcase the web identification methods in Figs 2 and 3 as well as the level of agreement across web finders in Fig. 7.

Table 1. An overview of the methods compared in this study.

Method	Web types	Input	Type	Main references
Adapted minimal spanning tree (MST)	Filaments	Haloes	Graph and percolation	Alpaslan et al. (2014a)
Bisous	Filaments	Haloes	Stochastic	Tempel et al. (2014, 2016)
FINE	Filaments	Haloes	Stochastic	González & Padilla (2010)
Tidal shear tensor (T-web)	All	Particles	Hessian	Forero-Romero et al. (2009)
Velocity shear tensor (V-web)	All	Particles	Hessian	Hoffman et al. (2012)
CLASSIC	All	Particles	Hessian	Kitaura & Angulo (2012)
NEXUS+	All	Particles	Scale-space, Hessian	Cautun et al. (2013)
Multiscale Morphology Filter-2 (MMF-2)	All except knots	Particles	Scale-space, Hessian	Aragón-Calvo et al. (2007a) Aragón-Calvo & Yang (2014)
Spineweb	All except knots	Particles	Topology	Aragón-Calvo et al. (2010c)
DisPerSE	All except knots	Particles	Topology	Sousbie (2011)
ORIGAMI	All	Particles	Phase space	Falck et al. (2012); Falck & Neyrinck (2015)
Multi-Stream Web Analysis (MSWA)	All	Particles	Phase space	Ramachandra & Shandarin (2015)

Galaxies that are too distant from filaments are reprocessed under a second MST that identifies smaller scale interstitial structures dubbed 'tendrils' (Alpaslan et al. 2014b). Tendrils typically contain a few tens of galaxies, and typically exist within voids, or bridge the gap between two filaments within underdense regions. The properties of galaxies in these structures are often similar to those in more dense filaments (Alpaslan et al. 2015).

Finally, galaxies that are beyond a distance q from tendrils are identified as isolated void galaxies. The distances r and q are selected such that the integral over the two-point correlation, $\int R^2 \xi(R)\,\mathrm{d}R$, of void galaxies is minimized. This definition of a void galaxy ensures that the algorithm identifies a population of very isolated galaxies; this differs from searching for void galaxies in low-density regions, which does allow for clustering.

4.2 Bisous (Tempel, Stoica and Saar)

The detection of cosmic-web filaments is performed by applying an object (marked) point process with interactions (the Bisous process; Stoica et al. 2005) to the spatial distribution of galaxies or haloes. This algorithm provides a quantitative classification that complies with the visual impression of the cosmic web and is based on a robust and well-defined mathematical scheme. More detailed descriptions of the Bisous model can be found in Stoica et al. (2007, 2010) and Tempel et al. (2014, 2016). A brief and intuitive summary is provided below.

The model approximates the filamentary web by a random configuration of small segments (cylinders). It is assumed that locally, galaxy conglomerations can be probed with relatively small cylinders, which can be combined to trace a filament if the neighbouring

cylinders are oriented similarly. An advantage of the approach is that it relies directly on the positions of galaxies and does not require any additional smoothing for creating a continuous density field.

The solution provided by the model is stochastic. Therefore, it has found some variation in the detected patterns for different Markov chain Monte Carlo (MCMC) runs of the model. On the other hand, thanks to the stochastic nature of the method simultaneously a morphological and a statistical characterization of the filamentary pattern is gained.

In practice, after fixing an approximate scale of the filaments, the algorithm returns the filament detection probability field together with the filament orientation field. Based on these data, filament spines are extracted and a filament catalogue is built in which every filament is represented by its spine as a set of points that defines the axis of the filament.

The spine detection follows two ideas. First, filament spines are located at the highest density regions outlined by the filament probability maps. Secondly, in these regions of high probability for the filamentary network, the spines are oriented along the orientation field of the filamentary network. See Tempel et al. (2014, 2016) for more details of the procedure.

The Bisous model uses only the coordinates of all haloes. These were analysed using a uniform prior for filament radius between 0.4 and 1.0 h^{-1} Mpc, which determines the scale of the detected structures. This scale has a measurable effect on properties of galaxies (Guo, Tempel & Libeskind 2015; Tempel & Tamm 2015; Tempel et al. 2015). Using the halo distribution, the Bisous model generates two fields – the filament detection and the filament orientation fields. These two fields are continuous and have a well-defined value at each point. To generate the data sets required by the comparison project, each grid cell on the target 100^3 mesh and each FOF halo was tagged as either part of a filament or not. For the visitmap[2] a threshold value 0.05 was used, which selects regions that are reasonably covered by the detected filamentary network. To exclude regions where the filament orientation is not well defined (e.g. regions at intersection of filaments), it is required that orientation strength parameter is higher than 0.7. The same values were used in previous studies (e.g. Nevalainen et al. 2015).

4.3 FINE (Gonzalez and Padilla)

The filamentary structure in the cosmic web can be found by following the highest density paths between density peaks. The Filament Identification using NodEs (FINE) method described in González & Padilla (2010) looks for filaments in halo or galaxy distributions.

The method requires halo/galaxy positions and masses (luminosities for galaxies), and we define as nodes, the haloes/galaxies above a given mass/luminosity. The mass of the nodes will define the scale of the filaments in the search. The smaller the node masses, the smaller the filaments that will be found between them.

The density field is computed using Voronoi Tessellations similar to Schaap & van de Weygaert (2000). The method looks first for a filament skeleton between any node pair by following the highest density path and a minimum separation; those two parameters characterize the filament quality. Filament members are selected by binding energy in the plane perpendicular to the filament; this condition is associated with characteristic orbital times. However, if one assumes a fixed orbital time-scale for all filaments, the resulting filament properties show only marginal changes, indicating that

the use of dynamical information is not critical for this criterion. Filaments detected using this method are in good agreement with Colberg et al. (2005) who use by-eye criteria.

In this comparison we define nodes as the haloes with masses above 5×10^{13} M$_\odot$, and the minimum density threshold for the skeleton search is five times the mean Voronoi density.

4.4 V-web: velocity shear tensor (Libeskind, Hoffman, Knebe and Gottlöber)

The cosmic web may be quantified directly using the cosmic velocity field, as suggested by Hoffman et al. (2012). This method is ideally suited to numerical simulations but may be applied to any cosmic velocity field, for example reconstructed ones from redshift or velocity data.

The method is similar to that suggested by Hahn et al. (2007a) but uses the shear field instead of the Hessian of the potential. In the linear regime, these two methods give similar results. First, a grid is superimposed on the particle distribution. A 'clouds in cells' (CIC) technique is used to obtain a smoothed density and velocity distribution at each point on the grid. The CIC of the velocity field is then fast Fourier transformed into k-space and smoothed with a Gaussian kernel. The size of the kernel determines the scale of the computation and must be at least equal to one grid cell (i.e. in this case we use a 256^3 grid and so $r_{\text{smooth}} \geq L_{\text{box}}/256$) in order to wash out artificial effects introduced by the preferential axes of the Cartesian grid. Using the Fourier Transform of the velocity field the normalized shear tensor is calculated as

$$\Sigma_{\alpha\beta} = -\frac{1}{2H_0} \left(\frac{\partial v_\alpha}{\partial r_\beta} + \frac{\partial v_\beta}{\partial r_\alpha} \right), \tag{1}$$

where α, β are the x, y, z components of the positions r and velocity v and H_0 is the Hubble constant. Note that the shear tensor is simply the symmetric part of the velocity deformation tensor (the antisymmetric part being the curl or vorticity, see Libeskind et al. 2013b,2014a). The shear tensor is then diagonalized and the eigenvalues are sorted, according to convention ($\lambda_1 > \lambda_2 > \lambda_3$). The eigenvalues and corresponding eigenvectors (e_1, e_2, e_3) of the shear field are obtained at each grid cell. Note that the eigenvectors (e_i's) define non-directional lines and as such the +/− orientation is arbitrary and degenerate.

A web classification scheme based on how many eigenvalues are above an arbitrary threshold may be carried out at each grid cell. If none, one, two or three eigenvalues are above this threshold, the grid cell may be classified as belonging to a void, sheet, filament or knot. The threshold may be taken to be zero (as in Hahn et al. 2007a) or may be fixed to another value, e.g. to reproduce the visual impression of the matter distribution; for the purposes of ΛCDM simulations, such as this one, the threshold is chosen to be 0.44 (Forero-Romero et al. 2009; Libeskind et al. 2012, 2013a, 2014b).

4.5 T-web: tidal shear tensor (Forero-Romero, Hoffman and Gottlöber)

This method (T-web; Forero-Romero et al. 2009) works on density field grids obtained either from numerical simulations or reconstructions from redshift surveys.

The method builds on the work by Hahn et al. (2007a). It also uses the Hessian of the gravitational potential

$$T_{\alpha\beta} = \frac{\partial^2 \phi}{\partial x_\alpha \partial x_\beta}, \tag{2}$$

---

[2] In mathematics the visitmap is also called a 'level set', and refers to a probabilistic filament detection map, see Heinrich, Stoica & Tran (2012).

where the physical gravitational potential has been normalized by $4\pi G\bar{\rho}$ so that ϕ satisfies the Poisson equation

$$\nabla^2\phi = \delta, \tag{3}$$

with δ the dimensionless matter overdensity, G the gravitational constant and $\bar{\rho}$ the average density of the Universe.

This tidal tensor can be represented by a real symmetric 3×3 matrix with eigenvalues $\lambda_1 > \lambda_2 > \lambda_3$ and eigenvectors $\boldsymbol{e}_1$, $\boldsymbol{e}_2$ and $\boldsymbol{e}_3$. The eigenvalues are indicators of orbital stability along the directions defined by the eigenvectors.

This method introduces a threshold λ_{th} to gauge the strength of the eigenvalues of the tidal shear tensor. The number of eigenvalues larger than the threshold is used to classify the cosmic web into four kinds of environments: voids (3 eigenvalues smaller than λ_{th}), sheets (2), filaments (1) and knots (0).

In practice, the density is interpolated over a grid using the particle data and a CIC scheme. The Poisson equation is solved in Fourier space to obtain the potential over a grid. At each grid cell the shear tensor is computed to obtain and store the corresponding eigenvalues and eigenvectors. The grid cell has a size of $\sim 1\,h^{-1}$Mpc and the threshold is fixed to be $\lambda = 0.2$ as suggested by previous studies that aim at capturing the visual impression of the cosmic web (Forero-Romero et al. 2009).

4.6 MMF/Nexus: the Multiscale Morphology Filter (Aragón-Calvo, Cautun, van de Weygaert and Jones)

The MMF/Nexus MMF technique (Aragón-Calvo et al. 2007a, 2010a; Cautun et al. 2013, 2014; Aragón-Calvo & Yang 2014) performs the morphological identification of the cosmic web using a *Scale-space formalism* that ensures the detection of structures present at all scales. The formalism consists of a fully adaptive framework for classifying the matter distribution on the basis of local variations in the density field, velocity field or gravity field encoded in the Hessian matrix in these scales. Subsequently, a set of morphological filters is used to classify the spatial matter distribution into three basic components, the clusters, filaments and walls that constitute the cosmic web. The final product of the procedure is a complete and unbiased characterization of the cosmic-web components, from the prominent features present in overdense regions to the tenuous networks pervading the cosmic voids.

Instrumental for this class of MMF cosmic-web identification methods is that it simultaneously pays heed to two principal aspects characterizing the web-like cosmic mass distribution. The first aspect invokes the Hessian of the corresponding fields to probe the existence and identity of the mostly anisotropic structural components of the cosmic web. The second, equally important, aspect uses a scale-space analysis to probe the multiscale character of the cosmic mass distribution, the product of the hierarchical evolution and buildup of structure in the Universe.

The scale-space representation of a data set consists of a sequence of copies of the data having different resolutions (Florack et al. 1992; Lindeberg 1998). A feature searching algorithm is applied to all of these copies, and the features are extracted in a scale-independent manner by suitably combining the information from all copies. A prominent application of the scale-space analysis involves the detection of the web of blood vessels in a medical image (Sato et al. 1998; Li, Sone & Doi 2003). The similarity to the structural patterns seen on megaparsec scales is suggestive. The MMF has translated, extended and optimized the scale-space technology to identify the principal characteristic structural elements in the cosmic mass and galaxy distribution. The final outcome of the MMF/Nexus

procedure is a field that at each location $\boldsymbol{x}$ specifies what the local morphological signature is, cluster node, filaments, wall or void. The MMF/Nexus algorithms perform the environment detection by applying the above steps first to knots, then to filaments and finally to walls. Each volume element is assigned a single environment characteristic by requiring that filament regions cannot be knots and that wall regions cannot be either knots or filaments. The remaining regions are classified as voids.

Following the basic version of the MMF technique introduced by Aragón-Calvo et al. (2007a), it was applied to the analysis of the cosmic web in simulations of cosmic structure formation (Aragón-Calvo et al. 2010a) and for finding filaments and galaxy–filament alignments in the SDSS galaxy distribution (Jones et al. 2010). The principal technique, and corresponding philosophy, has subsequently branched into several further elaborations and developments. In this survey, we describe the Nexus formalism developed by Cautun et al. (2013) and the MMF2 method developed by Aragón-Calvo & Yang (2014). Nexus has extended the MMF formalism to a substantially wider range of physical agents involved in the formation of the cosmic web, along with a substantially firmer foundation for the criteria used in identifying the various web-like structures. MMF-2 not only focusses on the multiscale nature of the cosmic web itself, but also addresses the nesting relations of the hierarchy.

4.6.1 NEXUS+ (Cautun, van de Weygaert and Jones)

The NEXUS+ version of the MMF/Nexus formalism (Cautun et al. 2013, 2014) builds upon the original MMF (Aragón-Calvo et al. 2007a, 2010a) algorithm and was developed with the goal of obtaining a more physically motivated and robust method.

NEXUS+ is the principal representative of the full NEXUS suite of cosmic-web identifiers (see Cautun et al. 2013). These include the options for corresponding multiscale morphology identifiers on the basis of the raw density, the logarithmic density, the velocity divergence, the velocity shear and tidal force field. NEXUS has incorporated these options in a versatile code for the analysis of cosmic-web structure and dynamics following the realization that they are significant physical influences in shaping the cosmic mass distribution into the complexity of the cosmic web.

NEXUS+ takes as input a regularly sampled density field. In a first step, the input field is Gaussian smoothed over using a Log-Gaussian filter (see Cautun et al. 2013) that is applied over a set of scales $[R_0, R_1, \ldots, R_N]$, with $R_n = 2^{n/2}R_0$. NEXUS+ then computes an environmental signature for each volume element.

The NEXUS suite of MMF identifiers pays particular attention to the key aspect of setting the detection thresholds for the environmental signature. Physical criteria are used to determine a detection threshold. All points with signature values above the threshold are valid structures. For knots, the threshold is given by the requirement that most knot-regions should be virialized. For filaments and walls, the threshold is determined on the basis of the change in filament and wall mass as a function of signature. The peak of the mass variation with signature delineates the most prominent filamentary and wall features of the cosmic web.

For the NEXUS+ implementation, the Delaunay Tessellation Field Estimator DTFE method (Schaap & van de Weygaert 2000; van de Weygaert & Schaap 2009) is used to interpolate the dark matter particle distribution to a continuous density field defined on a regular grid of size 600^3 (grid spacing of $0.33\,h^{-1}$ Mpc). NEXUS+ was applied to the resulting density field using a set

of seven smoothing scales from 0.5 to 4 h^{-1} Mpc (in increments of $\sqrt{2}$ factors). This resulted in an environment tag for each grid cell that, in a second step, was down sampled to the target 100^3 grid using a mass-weighted selection scheme. For each cell of the coarser grid, we computed the mass fraction in each environment using all the fine level cells (6^3 in total) that overlap the coarser one. Then, the coarser cell was assigned the environment corresponding to the largest mass fraction. Each FOF halo was assigned the web tag corresponding to the fine grid cell in which the halo centre was located.

4.6.2 MMF-2: Multiscale Morphology Filter-2 (Aragón-Calvo)

The MMF-2 implementation of the MMF formalism differs from the NEXUS formalism in that it focusses on the multiscale character of the initial density field, instead of that of the evolved mass distribution. In order to account for hierarchical nature of the cosmic web, MMF-2 introduces the concept of *hierarchical space* (Aragón-Calvo et al. 2010b; Aragon-Calvo & Szalay 2013). While the conventional scale-space approach emphasizes the scale of the structures, it does not address their nesting relations. To accomplish this, MMF-2 resorts to the alternative of *hierarchical space* (Aragón-Calvo et al. 2010b; Aragon-Calvo & Szalay 2013; Aragón-Calvo & Yang 2014).

Hierarchical space is created in the first step in the MMF-2 procedure (Aragón-Calvo et al. 2010b; Aragon-Calvo & Szalay 2013). It is obtained by Gaussian-smoothing the initial conditions, and in principal concerns a continuum covering the full range of scales in the density field. For practical purposes, however, a small set of linear-regime-smoothed initial conditions is generated. Subsequently, by means of an *N*-body code these conditions are gravitationally evolved to the present time.

By applying to linear-regime smoothing, *hierarchical space* involves density field Fourier modes that are independent. This allows the user to target specific scales in the density field before Fourier mode-mixing occurs. The subsequent gravitational evolution of these smooth initial conditions results in a mass distribution that contains all the anisotropic features of the cosmic web, while it lacks the small-scale structures below the smoothing scale. Dense haloes corresponding to these small scales are absent. This reduces the dynamic range in the density field and greatly limits the contamination produced by dense haloes in the identification of filaments and walls.

In line with the MMF procedure, for each realization in the hierarchical space a set of morphology filters is applied, defined by ratios between the eigenvalues of the Hessian matrix ($\lambda_1 < \lambda_2 < \lambda_3$, see Aragón-Calvo et al. 2007a). It also involves the applications of a threshold to the response from each morphology filter. This leads to a final product consisting of a set of binary masks sampled on a regular grid indicating which voxels belong to a given morphology at a given hierarchical level.

4.7 CLASSIC (Manti, Nuza and Kitaura)

The CLASSIC approach is based on performing a prior linearization to the cosmological density field and later a cosmic-web classification of the resulting matter distribution. The method is implemented in two steps: first, a linearization is made to better fulfil the mathematical conditions of the original idea of cosmic-web classification, which is based on a linear Taylor expansion of the gravitational field (see Zel'dovich 1974; Hahn et al. 2007a), and then, cosmological

structures are divided into voids, sheets, filaments and knots. The linearization is done using higher order Lagrangian perturbation theory as proposed by Kitaura & Angulo (2012). In this framework, a given density field can be expressed as the sum of a linear component and a non-linear component that are tightly coupled to each other by the tidal field tensor. The cosmic-web classification is performed on a grid cell in a similar way as suggested by Hahn et al. (2007a), i.e. counting the number of eigenvalues of the Hessian of the gravitational potential above a given threshold (see also Forero-Romero et al. 2009). In particular, the threshold adopted was chosen to obtain a volume filling fraction (VFF) of voids of about 70 per cent as done by Nuza et al. (2014) for their reconstruction on the local universe based on peculiar velocity fields. As a result, the corresponding VFFs of sheets, filaments and knots are uniquely determined by this choice.

4.8 Spineweb (Aragón-Calvo, Platen and van de Weygaert)

The Spine method (Aragón-Calvo et al. 2010c) produces a characterization of space based on the topology of the density field, catalogues of individual voids, walls and filaments and their connectivity. Its hierarchical implementation (Aragón-Calvo et al. 2010a; Aragon-Calvo & Szalay 2013) allows us to describe the nesting properties of the elements of the cosmic web in a quantitative way. The Spine can be applied to both simulations and galaxy catalogues with minimal assumptions. Given its topological nature, it is highly robust against geometrical deformations (e.g. fingers of God or polar grid sampling) as long as the topology of the field remains unchanged.

The Spine method extends the idea introduced in the watershed void finder (Platen et al. 2007) to identify voids as the contiguous regions sharing the same local minima. Walls are then identified as the 2D regions where two voids meet and filaments correspond to the 1D intersection of two or more walls. Nodes correspond to the intersection of two or more filaments but due to the finite size of voxels in practice they are difficult to recover and therefore we merge them with the filaments into the filament-node class.

The Spine method can be extended to a fully hierarchical analysis as explained in Aragón-Calvo et al. (2010a) and Aragon-Calvo & Szalay (2013). In this approach, void regions are identified at several hierarchical levels (see MMF-2 method), then voids identified at large scales (high in the hierarchical space) are reconstructed in terms of the voids they contain at smaller scales in order to recover their original boundaries lost by the smoothing procedure used to create the hierarchical space. From the reconstructed voids, we compute the watershed transform and identify walls and filament nodes as described above.

We use the fact that walls are the intersection of two voids to identify voxels belonging to a unique wall (voxels at the boundary between the same pair of walls). The same can be done for filaments in order to obtain a catalogue of voids, walls and filaments. The same connectivity relations can be used to reconstruct the full graph describing the elements of the cosmic web.

4.9 DisPerSE (Sousbie)

DISPERSE is a formalism designed for analysing the cosmic web, and in particular its filamentary network, on the basis of the topological structure of the cosmic mass distribution (Sousbie 2011; Sousbie et al. 2011). The elaborate framework of DISPERSE is based on three mathematical and computational pillars. These are Morse

theory (Morse 1934; Milnor 1963), Discrete Morse theory (Forman 1998; Gyulassy 2008) and the Delaunay Tessellation Field Estimator DTFE (Schaap & van de Weygaert 2000; van de Weygaert & Schaap 2009; Cautun & van de Weygaert 2011). The formalism uses three concepts in computational topology: Persistent Homology and Topological Simplification (Edelsbrunner, Letscher & Zomorodian 2002; Gyulassy 2008; Edelsbrunner & Harer 2010). These are used for the removal of noise and the selection of the significant morphological features from a discretely sampled cosmic mass distribution.

DISPERSE analyses and characterizes the cosmic web in terms of a spatial segmentation of space defined by the singularity structure of the cosmic mass distribution, the *Morse complex*. The morphological components of the cosmic web are identified with the various *k*-dimensional manifolds that outline this uniquely defined segmentation. Filaments are identified with the ascending 1-manifold. Voids, walls and clusters are identified with the ascending 3, 2 and 0 manifolds (also see Aragón-Calvo et al. 2010c; Shivashankar et al. 2016). DISPERSE follows earlier applications of Morse theory to structural classification in astrophysical data sets (Colombi et al. 2000). The immediate precursor to DISPERSE is the skeleton formalism (Sousbie et al. 2008a,b; Sousbie, Colombi & Pichon 2009).

Morse theory, which forms the basis for DISPERSE, looks at the singularity structure of the density field $f(x)$. It leads to the translation of the spatial distribution and connectivity of maxima, minima and saddle points in the density fields into a geometric segmentation of space that is known as the *Morse complex*. This is a uniquely defined segmentation of space in a spatial tessellation of cells, faces, edges and nodes defined by the singularities and their connections by integral lines. The *index* of a non-degenerate critical point is the number of negative eigenvalues of its Hessian: a *minimum* of a field *f* has index 0, a *maximum* has index 3, while there are two types of *saddles*, with index 1 and 2. Morse theory captures the connectivity of a field *f* via the flowlines defined by the field gradient ∇*f*, the *integral lines*. The field minima and maxima are the divergence and convergence points of these lines. It leads to a natural segmentation of space into distinct regions of space called ascending and descending manifolds. The *ascending k*-manifold of a critical point *P* defines the *k*-dimensional region of space defined by the set of points along integral lines that emanate from origin *P*. Conversely, the *descending m*-manifold of a critical point *P* is the *m*-dimensional region of space defined by the set of points along integral lines for which *P* is the destination.

Since astronomical data sets (*N*-body simulations, galaxy catalogues, etc.) are discrete and intrinsically noisy tracers of the density field, DISPERSE utilizes *Discrete Morse theory* (see e.g. Forman 1998). It consists of a combinatorial formulation of Morse theory in terms of intrinsically discrete functions defined over a simplicial complex.[3] A well-known example is the Delaunay tessellation 𝒟 (van de Weygaert 1994; Okabe et al. 2000). DISPERSE uses the Delaunay tessellation, and specifically its role as functional basis in the DTFE formalism (Schaap & van de Weygaert 2000; van de Weygaert & Schaap 2009; Cautun & van de Weygaert 2011). DISPERSE uses the DTFE density estimate at each sample point, while it assigns a density value $f(\sigma_k)$ to each simplex σ_k of the Delaunay simplicial complex 𝒟. On the basis of these values, and the mutual connections between the various simplices, one may identify dis-

crete simplicial analogues to the singularity points, gradient vector field, integral lines and Morse complex (see e.g. Gyulassy 2008; Sousbie 2011, for a detailed treatment).

The finite sampling of the density field introduces noise into the detection of structural features. Instead of resorting to a simplistic feature-independent filtering operation, which tends to suppress or even annihilate real structural features, DISPERSE uses persistent homology (Edelsbrunner et al. 2002; Edelsbrunner & Harer 2010). Topological persistence is the language that allows the identification of features according to their significance (Edelsbrunner et al. 2002). Persistence theory defines a topological criterion for the birth and the death of features, and the persistence of a feature, i.e. its significance, is quantified according to the interval between its appearance and demise. For the removal of insignificant features, DISPERSE augments the persistence measurement with the *topological simplification* of the discrete Morse complex (Edelsbrunner et al. 2002; Gyulassy 2008), consisting of an ordered elimination of simplicial singularities and their connections.

The final product of DISPERSE is a simplicial complex with appropriately adapted gradient lines and corresponding ascending manifolds. It provides a map of the morphological structures that make up the web-like arrangement of galaxies and mass elements on megaparsec scales, identified in terms of the ascending manifolds of a discrete and topologically filtered Morse complex. Most outstanding is the filamentary network corresponding to the index 1 ascending manifolds.

4.10 ORIGAMI (Falck and Neyrinck)

The gravitational collapse of dark matter can be thought of as the 6D distortion, in phase-space, of an initially flat 3D manifold. Folds in this manifold occur at caustics and mark out regions of shell-crossing within which the velocity field is multivalued. ORIGAMI uses the association between shell-crossing and non-linear structure formation to identify the different components of the cosmic web, which are fundamentally distinguished by the dimensionality of their collapse: haloes are collapsing along three orthogonal axes, filaments along two, walls along one and voids are instead expanding (Falck et al. 2012).

ORIGAMI determines whether, and in how many dimensions, shell-crossing has occurred for each dark matter particle in the simulation by checking whether particles are out of order with respect to their initial orientation on the Lagrangian grid. For computational efficiency, ORIGAMI currently requires grid instead of 'glass' initial conditions; we check for crossings along the Cartesian grid of the simulation box and additionally along three sets of rotated axes (for details, see Falck et al. 2012). For each particle, we test for crossings with respect to all particles along a given Lagrangian axis, extending up to 1/4th of the box size in each direction. The number of orthogonal axes along which shell-crossing is detected is counted for each set of axes, and the maximum among all sets of axes is the particle's morphology index: 0, 1, 2 and 3 crossings indicate void, wall, filament and halo particles, respectively.

ORIGAMI thus provides a cosmic-web classification for each dark matter particle in the simulation without using a density parameter or smoothing scale. Since we apply no smoothing or otherwise impose a scale, the cosmic-web classification thus depends on the simulation resolution: there is more small-scale structure present in higher resolution simulations, so ORIGAMI identifies a higher fraction of halo particles and lower fraction of void particles as resolution increases (Falck et al. 2012; Falck & Neyrinck 2015).

---

[3] In essence, a simplicial complex is a geometric assembly of cells, faces, edges and vertices marking a discrete map of the volume. Cells, faces, edges and nodes/vertices are 3D, 2D, 1D and 0D simplices.

For the purpose of this comparison project, the cosmic-web identification for each particle is converted to classification on a regular grid as follows: for each grid cell, select the morphology having the maximum number of particles as the morphology of that cell. If there are no particles in a cell, then that cell may be designated as a void. If there is a tie, with two morphologies having the maximum number of particles, assign the lower morphology to the cell (i.e. void < wall < filament < halo). Ties can be quite common between void and wall particles, especially for low-resolution simulations and fine grids.

Because of the particle-based web definition, most halo particles identified by ORIGAMI correspond to haloes identified by FOF. In previous work (Falck et al. 2014), the web environment of ORIGAMI haloes is defined according to the morphology of particles that neighbour the haloes, but this does not work for FOF haloes since the neighbour particles of FOF haloes are most often included as part of ORIGAMI haloes. For this comparison project, then, we classify each FOF halo according to the web identification of the grid cell it is in.

4.11 Multi-Stream Web Analysis (Shandarin and Ramachandra)

The growth of CDM density perturbations results in the emergence of regions where the velocity has distinct multiple values. These regions are also of high densities. The DM web can be viewed as a multistream field. For example, voids are the regions where the velocity field has a single value. This is because no gravitationally bound DM object can form prior to origin of shell crossing, which corresponds to the formation of regions with at least three streams. Three-stream flows associated with Zel'dovich's pancakes are gravitationally bound only in one direction, roughly perpendicular to the pancake. Filaments are bound in two directions orthogonal to the filament, and haloes are of course fully bound. The generic geometrical structures of the web, i.e. walls aka pancakes, filaments and haloes, cannot be uniquely defined by any particular threshold of the multistream field, which is also true for the density field. Generally all three-stream regions belong to the walls, but the transition to the filaments and to the haloes may occur at different levels.

The multistream field can be easily computed from the final and initial coordinates of the particles in cosmological *N*-body simulations (Abel et al. 2012; Shandarin et al. 2012). A cold collisionless matter represents an extremely thin 3D sheet called a Lagrangian submanifold in 6D space made by three initial and three final coordinates at a chosen state of the simulation. Similarly to the 3D sheet in the 6D phase space, the Lagrangian submanifold contains full dynamic information about the system. It needs to be tetrahedralized only once by using initial positions of the particles on a regular grid as vertices of the tetrahedra. During the following evolution the tessellation remains intact. It always remains continuous, and its projection in 3D coordinate space fully tiles it at least by one layer in voids and many times in the web regions. The tetrahedra during the evolution are deformed, but the deformation has no effect on the connectivity assignments between the particles. The number of streams can be computed on an arbitrary set of spatial points by simply counting how many tetrahedra contain a given point. The first study of the multistream environment of DM haloes has been recently described in Ramachandra & Shandarin (2015).

Delineating the web components (walls, filaments and haloes) in multistream fields is not straightforward, and could be done using various approaches. By studying the scaling of multistream variation around dark matter haloes, Ramachandra & Shandarin (2015) showed that the geometries of structures change from sheets to filaments at a multistream value of $n_{str} \gtrsim 17$. The next transition from filaments to knots is seen at around $n_{str} \gtrsim 90$ – which also roughly corresponds to the virial mass density $\Delta_{vir} = 200$. These thresholds are heuristic – the analysis may have to be repeated for different simulations for the calibration of thresholds. On the other hand, local Hessian-based geometric methods were recently used to identify multistream structures by Ramachandra & Shandarin (2017). This approach hints towards a portrait of structures in multistream fields that are free of ad hoc thresholds. For instance, the haloes could be identified simply as convex surfaces enclosing a local maxima of the multistream field (Ramachandra & Shandarin, in preparation).

A summary of the classification scheme used for this comparison project is as follows: voids are simply the regions with $n_{str} = 1$. The web components are delineated by utilizing the first approach of calibrating thresholds, i.e. sheets: $3 \leq n_{str} < 17$, filaments: $17 \leq n_{str} < 90$ and knots: $n_{str} \geq 90$.

5 COMPARISON AND RESULTS

Here, we present a visual and quantitative comparison of the different methods. We focus on comparing general features of the cosmic web: mass and VFFs, density distributions and halo mass functions in each environment. As already mentioned, all methods were applied to the same simulation and they all used, depending on the method, either the dark matter particle distribution or the FOF halo catalogue.

5.1 Visual comparison

We begin our analysis by performing a visual comparison of the various web finders. Figs 2 and 3 show the environments returned by the web identification methods that took part in the comparison. Each panel shows the same 2 h^{-1} Mpc thick slice through the simulation box. Broadly speaking, there are two types of methods: the ones that return multiple cosmic-web environments (i.e. voids, sheets, filaments and possibly knots; these are shown in the Fig. 2) and the ones that identify only filaments (shown in Fig. 3). Among the first type, DISPERSE, MMF and Spineweb do not identify knots. For the second type of methods, we show either the grid cells identified as filaments (the Bisous method) or the positions of the haloes associated with filaments for the methods that did not return a web classification for each volume element (the FINE and MST methods). A number of general points are immediately visible from the inspection of Figs 2 and 3 (in no particular order):

(i) DISPERSE provides no knots, and its filaments are relatively thick compared to the other methods.

(ii) MMF-2 and Spineweb fill much of the simulation's volume with sheets and filaments.

(iii) ORIGAMI ascribes much of the overdense volume as knots – owing primarily to the fact that these regions contain haloes that have undergone shell crossing along three orthogonal axes.

(iv) The Hessian methods (NEXUS+, T-web, V-web and CLASSIC) have a mix of knots, filaments and sheets, with voids dominating the underdense volume.

(v) The Bisous model and MST seem more or less agree with each other, whereas the FINE method ascribes far fewer haloes to filaments.

It is important to note that some of these methods (specifically NEXUS+, MMF-2, T-web and V-web) have been designed, to various degrees, to reproduce the visual impression of the cosmic web.
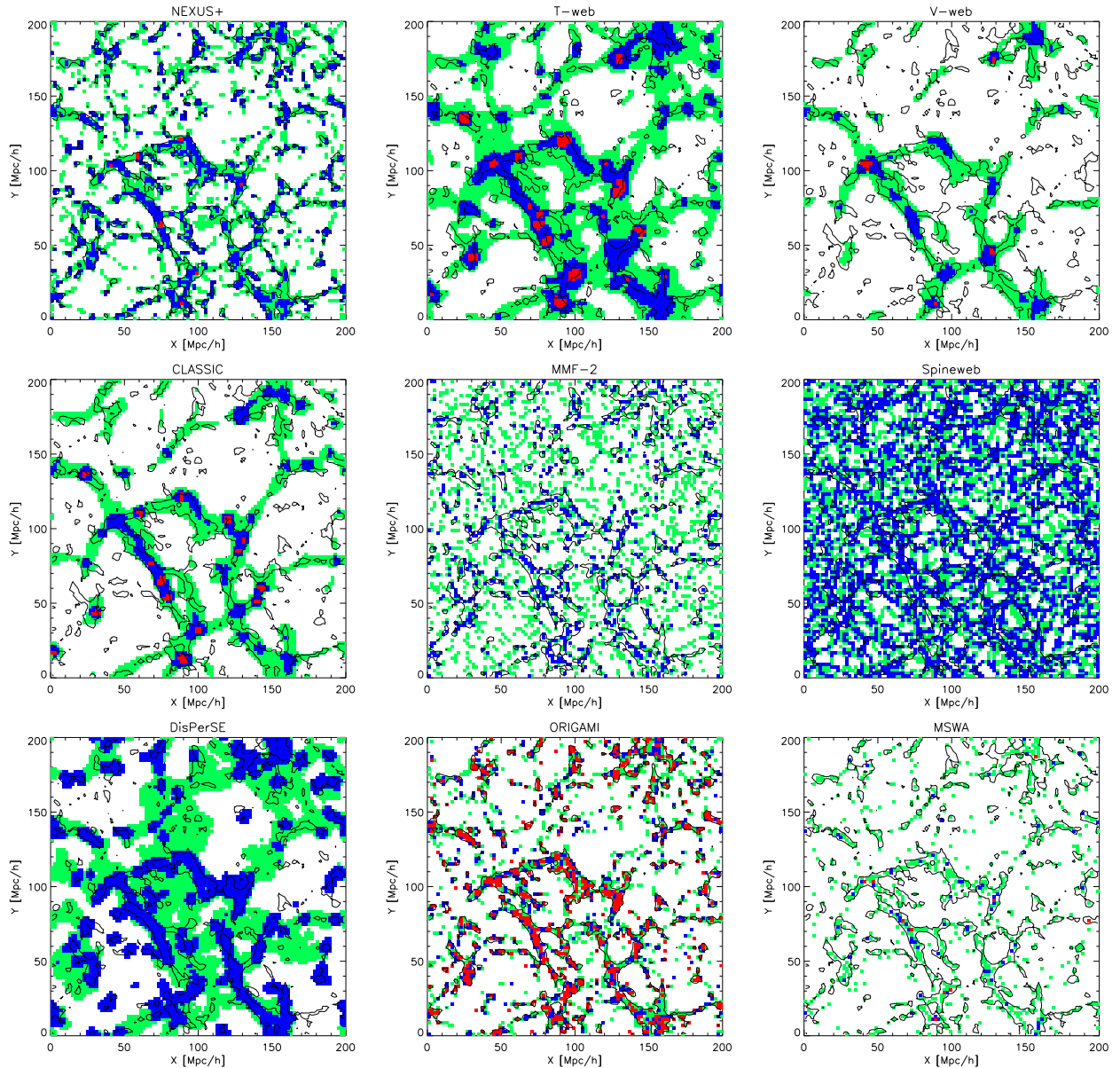
Figure 2. Visual comparison of environments as detected by the different cosmic-web finders. All panels show a thin, $2\,h^{-1}$ Mpc thick slice, where the various colours indicate: knots (red), filaments (blue), walls (green) and voids (white). Each panel has a set of solid lines that indicate the $\delta = 0$ contours (see the density distribution in Fig. 1). The simulation is purposefully coarse grained with cells of size $2\,h^{-1}$Mpc, as it is on this scale that the methods returned a classification.

Furthermore, given that voids are by definition underdense regions, it is ideologically unlikely that a given method would be designed to identify clusters deep inside voids.[4]

5.2 Density PDF

The relationship between the cosmic web and the density field can be quantified by studying the probability distribution function (PDF) of the density field for each volume element (grid cell) as a function of web environment. This is shown in Fig. 4, where the total density PDF for this simulation (computed on a regular grid

with cell spacing of $2\,h^{-1}$ Mpc) is shown in black and is the same in all panels; we quantify the density by normalizing to the mean density of the universe, $\delta = \rho/\bar{\rho}$. Note that only those methods that assign web classification to volume elements are included here – the FINE and MST methods assign a cosmic-web environment only to haloes and are therefore excluded. The median of each PDF is denoted by the corresponding arrow.

5.2.1 Knots

In Fig. 4(a), we show that knots are characterized by a wide variety of environmental densities. Although the T-web, V-web and CLAS-SIC roughly agree, they differ substantially from the fourth Hessian method, NEXUS+, which has a much narrower and higher distribution of densities. Indeed, NEXUS+ is in closer agreement with
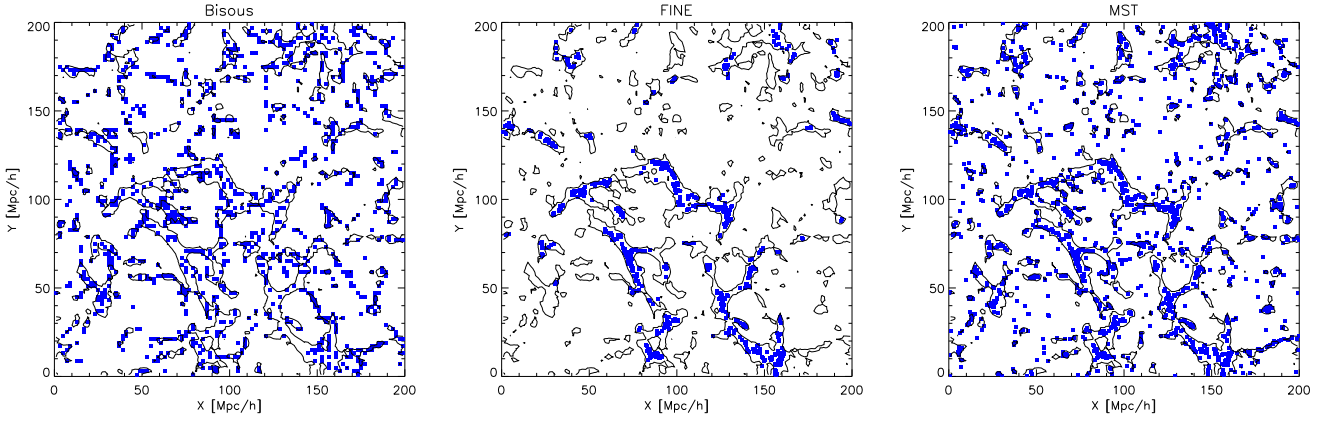
---

[4] The measure of a density depends on scale: large enough volumes that include relatively small overdensities can, on average, be well below the mean density and thus considered voids.

Figure 3. Same as Fig. 2 but for the three methods that identify only filaments.
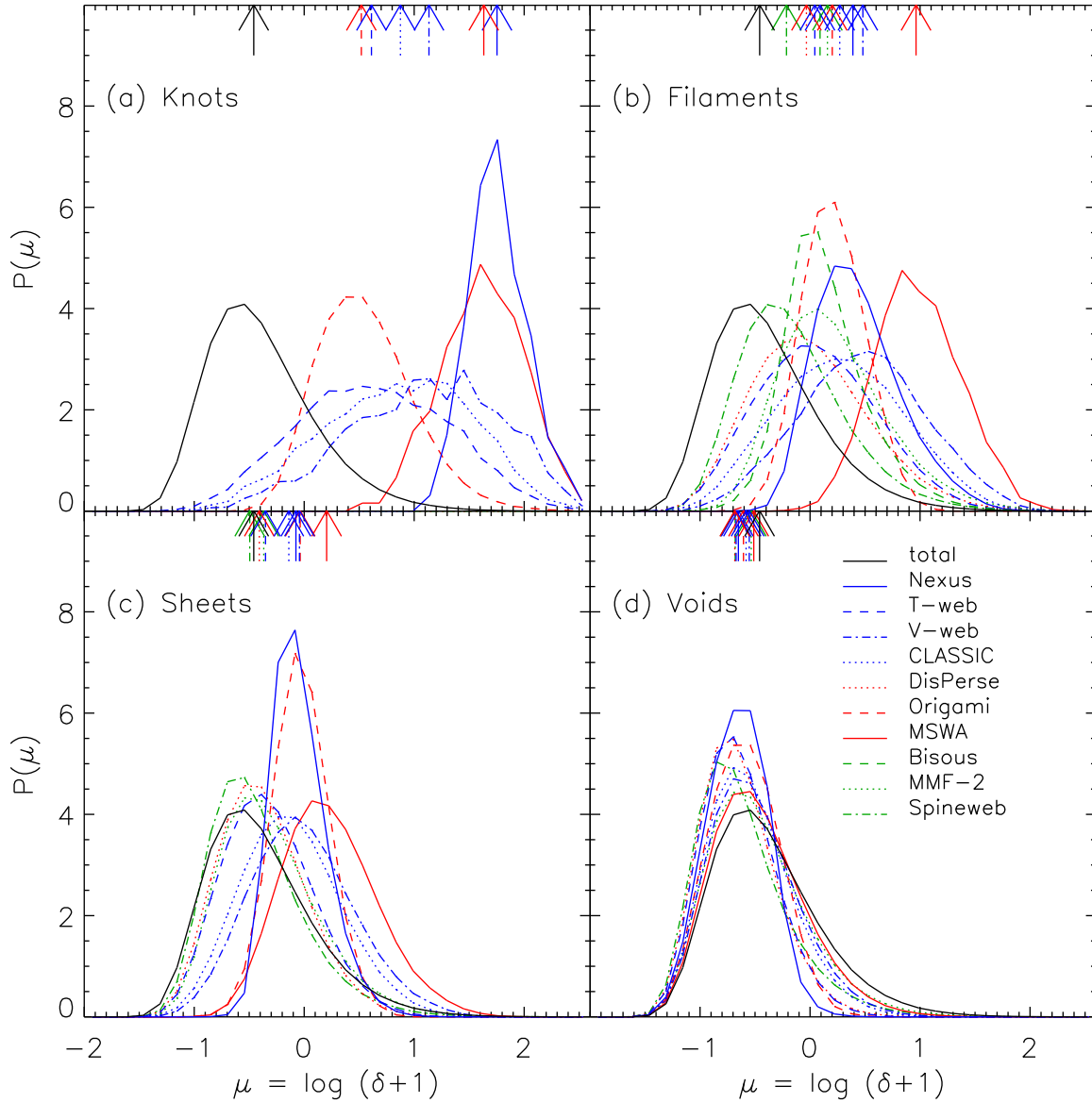

Figure 4. Comparison of the density contrast, $1 + \delta$, PDF as a function of environment for the different cosmic-web finders. The panels show the density PDF for: knots (top-left), filaments (top-right), sheets (bottom-left) and voids (bottom-right). The vertical arrows indicate the median of each distribution. Each PDF is normalized to unity and thus does not correspond to the VFF.

Multi-Stream Web Analysis (MSWA). ORIGAMI peaks at roughly the same density as V-web, although it is a little narrower.

Perhaps the strongest conclusion we can draw from Fig. 4(a) is that the local density by itself is a poor proxy for being considered a knot by any given method. Or, conversely, where knots are found, their density may differ by an order of magnitude or more.

5.2.2 Filaments

In Fig. 4(b), we show the PDF of densities for cells identified as filaments. Qualitatively, the picture is similar to that for knots, but pushed to slightly lower densities. There also appears to be a weak convergence of the median density among methods. Namely, although the widths of the PDF are similar, their medians are more strongly in agreement (with the exception of MSWA), and span less than an order of magnitude. MSWA stands out here in labelling higher density cells as filamentary; the Bisous model (the only filament-only model that can participate in this test) closely resembles ORIGAMI, while the PDFs of three of the Hessian methods (T-web, V-web and CLASSIC) have similar shapes but are offset with respect to each other. The PDF of Spineweb peaks at the lowest density.

5.2.3 Sheets

The density PDF for cells labelled as sheets, shown in Fig. 4(c), displays more coherence than those of knots or filaments. Despite the PDFs still varying widely among the web finders, the median densities of the PDFs are roughly similar and take values around $\delta = 0$. The median of the set of density PDFs moves to lower values, although, like the PDFs for knots and filaments, there is still a wide variety of permissible environments. Three pairs of methods produce nearly identical PDFs: NEXUS+ and ORIGAMI, DISPERSE, T-web, and MMF-2, and V-web and CLASSIC. Again, the PDF of Spineweb peaks at the lowest density.

5.2.4 Voids

The best agreement between methods is found in regions denoted as voids, as shown in Fig. 4(d). The void density PDFs show less diversity and generally have the same shape. The spread in medians is small: less than 0.2 dex. As voids purport to be the most underdense regions in the universe, they also make up the greatest fraction of the simulation's volume (as can be inferred by the overlap between the void density PDF and the total density PDF). It can thus be said that the methods studied here all agree that the majority of the simulation volume is indeed categorized as void.

5.2.5 Trends in the density PDFs

The cosmic-web classification is layered: knots are embedded in filaments, which, in turn, reside in sheets, which, in turn, constitute the boundaries between different void basins. As our analysis of the cosmic web moves from knots to voids, the median of the density distribution of each method and for each web type moves to lower values *in tandem.* Although for a given web type there may be a wide variety of permissible density environments across the analysed methods, each method follows a similar trend. The peak of the density PDF moves to lower and lower densities, with most methods converging in the lowest density and most abundant environment in the simulation: voids.

5.3 Mass and volume fraction

We continue the cosmic web finder's comparison with a study of the VFFs and mass filling fractions that are ascribed to a specific cosmic-web type. These quantities are shown in Fig. 5 for knots, filaments, sheets and voids. The mass fraction is found by summing up the particles in all the cells with the same cosmic-web type and dividing by the total number of particles in the simulation. The volume fraction is found by counting all the cells with the same cosmic-web type and dividing by the total number of cells. Note that for these tests we have a 100^3 grid with $(2\ h^{-1}\ \mathrm{Mpc})^3$ cells.

(i) *Knots*: as ORIGAMI makes no distinction between knots and haloes, it is perhaps unsurprising that this method finds that nearly half the simulation's mass is confined in $\sim$7 per cent of the volume. Most other methods tag far fewer cells as knots, claiming they constitute below $\sim$1 per cent of the volume with between 10 per cent and 20 per cent of the mass. Interestingly the mass–volume fraction relation for knots follows a fairly tight linear proportionality – the more mass found in knots, the more volume, regardless of method used.

(ii) *Filaments*: a similar, but slightly weaker proportionality between mass and volume fraction is found for filament regions. Here, Spineweb and DISPERSE place roughly 60 per cent of the simulations mass in filaments which occupy some $\sim$35 per cent and $\sim$25 per cent of the simulation volume, respectively. Unlike knots, there is considerably more spread in the relationship between mass and volume fractions amongst the methods, although a linear relationship is still discernible to the eye. Similar to knots, MSWA continues to place virtually none of the volume and roughly $\sim$10 per cent of the simulation's mass in filaments. The Bisous model – the only one of the filament-only models that can participate in this comparison – finds very similar filament VFFs and mass filling fractions as CLASSIC, V-web and MMF-2, with some $\sim$5 per cent of the simulations volume and $\sim$30 per cent of the simulations mass labelled as filaments. To summarize, the filament VFF spans from virtually nothing (MSWA) to more than a third of the volume (Spineweb); while the filament mass filling fraction spans roughly double that range, from $\sim$10 per cent (MSWA) to $\sim$60 per cent (DISPERSE).

(iii) *Sheets*: the spread of the sheet mass filling fraction is quite tight, with most methods assigning $\sim$30 per cent $\pm$ 5 per cent of the total mass to sheets (with the exception of ORIGAMI and MMF-2, which find lower values). However, the sheet VFFs vary substantially between methods, ranging from less than $\sim$10 per cent for MWSA to more than 40 per cent for T-web. As in knots and filaments, MWSA continues to assign only a small volume fraction to sheets.

(iv) *Voids*: The volume fraction associated with voids shows three distinct groups: three methods with $\sim$40 per cent (DISPERSE, Spineweb and T-web), five with $\sim$70 per cent (NEXUS+, ORIGAMI, V-web, MMF-2 and CLASSIC) and one with $\sim$90 per cent (MSWA). For the first group of finders (DISPERSE, Spineweb and T-web), the mass fraction is more or less the same at around 10–15 per cent. For the second group (NEXUS+, ORIGAMI, V-web, MMF-2 and CLASSIC), the mass fraction in voids spans a large range from $\sim$15 per cent for NEXUS+ to $\gtrsim$ 50 per cent for MMF-2. In general it is apparent that the mass fraction assigned to void regions spans a large range. It is interesting to note how the void mass filling fractions of these methods have flipped compared to their estimate for the filament mass fraction.
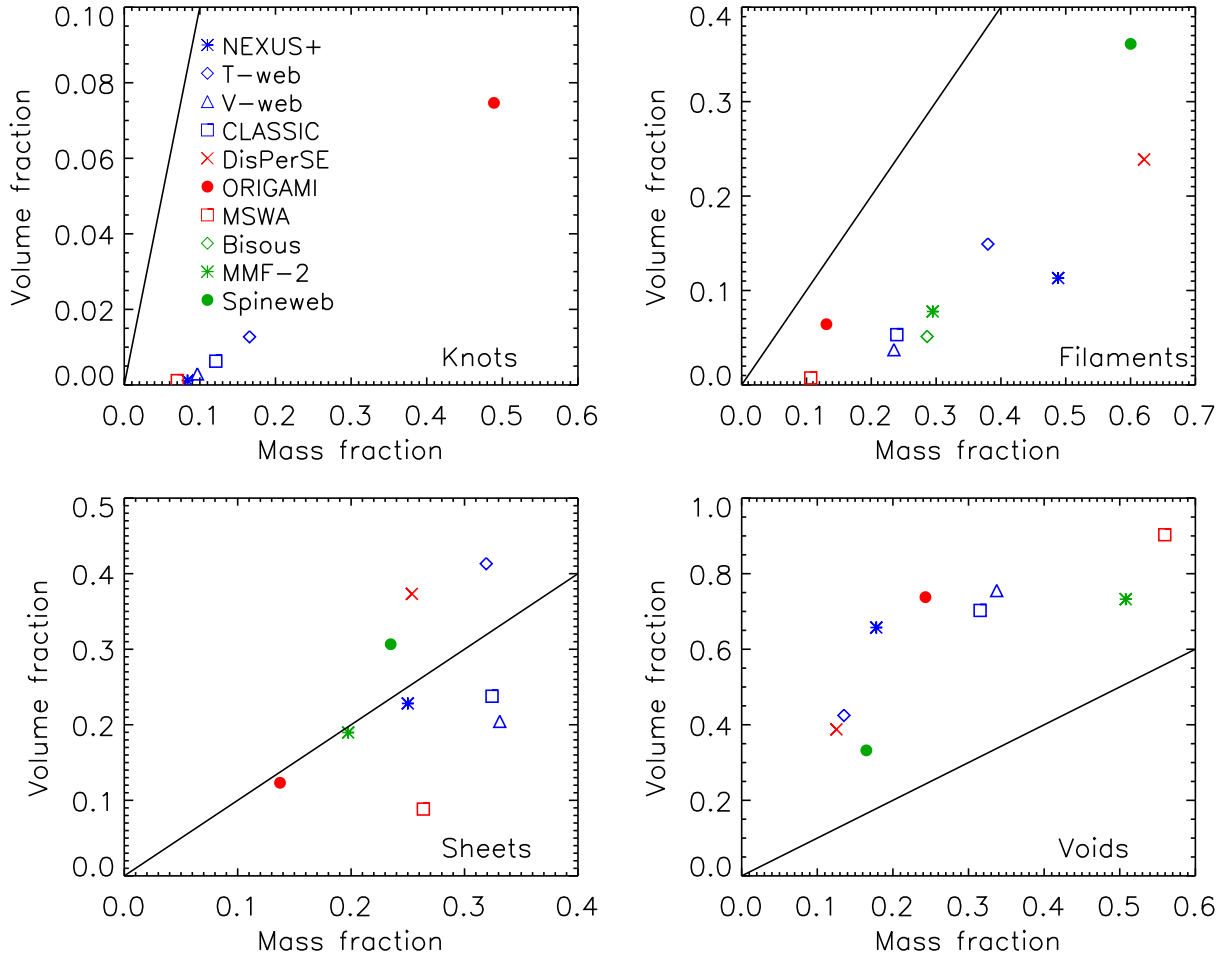
Figure 5. The mass and VFF of knots (top-left), filaments (top-right), sheets (bottom-left) and voids (bottom-right) as identified by the various cosmic-web finders. These quantities were computed using a regular grid with a cell spacing of $2\,h^{-1}$ Mpc. The solid line shows the mean filling fraction, i.e. a slope of unity, where the VFF equals the mass filling fraction. Namely, points above this line lie in underdensities, points below it in overdensities.

Table 2. The fraction of the volume, total mass and mass in haloes (with $M_{halo} > 10^{11}\,h^{-1}\,M_\odot$) in each web environment for each method. Note that two methods (MST and FINE) identify filaments in the halo (not particle) distribution and do not provide an environment characterization of individual volume elements. MST assigns all haloes not ascribed to a filament as being in voids.

| Method | Volume fraction (cells) | | | | Mass fraction (cells) | | | | Mass fraction (haloes) | | |
	Knots	Filaments	Sheets	Voids	Knots	Filaments	Sheets	Voids	Knots	Filaments	Sheets	Voids
MST	–	–	–	–	–	–	–	–	–	0.941	–	0.023
Bisous	–	0.051	–	–	–	0.286	–	–	–	0.377	–	–
FINE	–	–	–	–	–	–	–	–	–	0.411	–	–
V-web	0.003	0.034	0.204	0.755	0.097	0.235	0.331	0.337	0.231	0.317	0.293	0.159
T-web	0.013	0.149	0.413	0.425	0.166	0.380	0.319	0.135	0.328	0.415	0.211	0.045
CLASSIC	0.006	0.053	0.238	0.703	0.121	0.239	0.324	0.315	0.271	0.276	0.290	0.163
NEXUS+	0.001	0.113	0.228	0.657	0.084	0.488	0.250	0.178	0.245	0.658	0.088	0.006
MMF-2	–	0.078	0.190	0.732	–	0.295	0.197	0.508	–	0.909	0.072	0.019
Spineweb	–	0.361	0.307	0.332	–	0.600	0.235	0.165	–	0.971	0.027	0.001
DisPerSE	–	0.239	0.373	0.388	–	0.621	0.254	0.125	–	0.797	0.158	0.044
ORIGAMI	0.074	0.064	0.123	0.738	0.489	0.131	0.137	0.243	0.898	0.067	0.024	0.010
MSWA	0.001	0.007	0.088	0.903	0.070	0.106	0.264	0.560	0.641	0.219	0.130	0.009

In summary, the various methods predict fairly large ranges for the volume and mass fractions assigned to a given web type. Given the substantial differences in how these methods identify the web components, it is not very surprising that there are large discrepan-cies in these fractions. That said, in each plot of Fig. 5, clusters of methods can be identified which have similar values of either the volume fraction, mass fraction or both. The values for the mass and volume fractions are shown in the first two columns of Table 2.
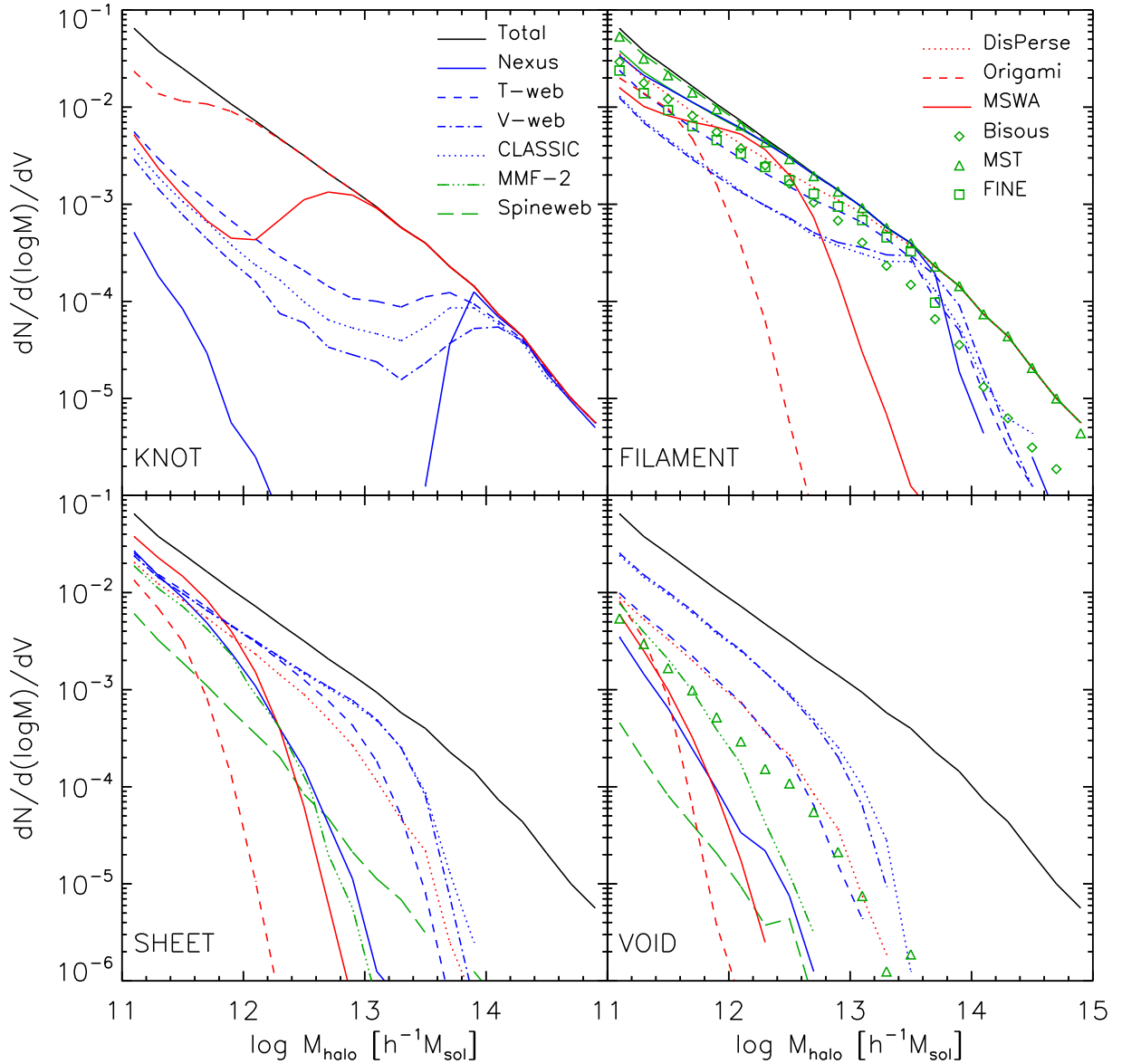
Figure 6. Comparison of the halo mass function as a function of environment for the various cosmic-web finders. The panels show the mass function for: knots (top-left), filaments (top-right), sheets (bottom-left) and voids (bottom-right). The black solid line shows the total halo mass function.

5.4 Halo assignment and mass functions

We now compare how the web environment assigned to haloes varies across cosmic-web finders. For most methods, each halo is assigned the cosmic-web environment of the cell in which its centre is located in. For the filament-only methods (Bisous, FINE, and MST), the methods themselves directly identify which haloes are part of a filamentary structure.

In Fig. 6, we show the halo mass function for the entire halo sample and for each web type. We find a mixed picture, with substantial variations in the halo mass function of web types. Despite this, there are also agreements. For example, all the methods place the most massive haloes (i.e. $M \gtrsim 10^{14} \, \mathrm{M_\odot}$) into knots. Similar trends are visible in how the filament halo mass function behaves – the mass functions are similarly valued at low masses and show a 'knee' that precipitates a quick decline in the mass function. The agreement of mass functions in filaments is strongest (except the phase-space methods, ORIGAMI and MSWA), and the

shape of the halo mass function in filaments is the closest one to the total halo mass function. Indeed, MMF-2 and Spineweb place nearly all haloes in filaments: the green dashed and dot–dashed curves are only visibly separate from the black line below $\sim 10^{12.5} \, h^{-1} \, \mathrm{M_\odot}$.

The last column of Table 2 shows how much mass is locked up in haloes of a given web type for each web finder. The four Hessian methods (NEXUS+, T-web, V-web and CLASSIC) agree that around 20–30 per cent of mass in haloes is found in knot haloes. This is dramatically different from DISPERSE, MMF-2 and Spineweb which do not identify haloes as belonging to knots, and the phase-space methods (ORIGAMI and MSWA), which place the bulk of halo mass in knots. It is interesting to note that the methods that do not identify knots, but do identify filaments, sheets and voids (Spineweb, MMF-2 and DISPERSE) place the overwhelming bulk of halo mass in filaments (with $\gtrsim 80$ per cent of all halo mass in filaments). All methods also agree that haloes in voids have the least amount of total halo mass, although they disagree on
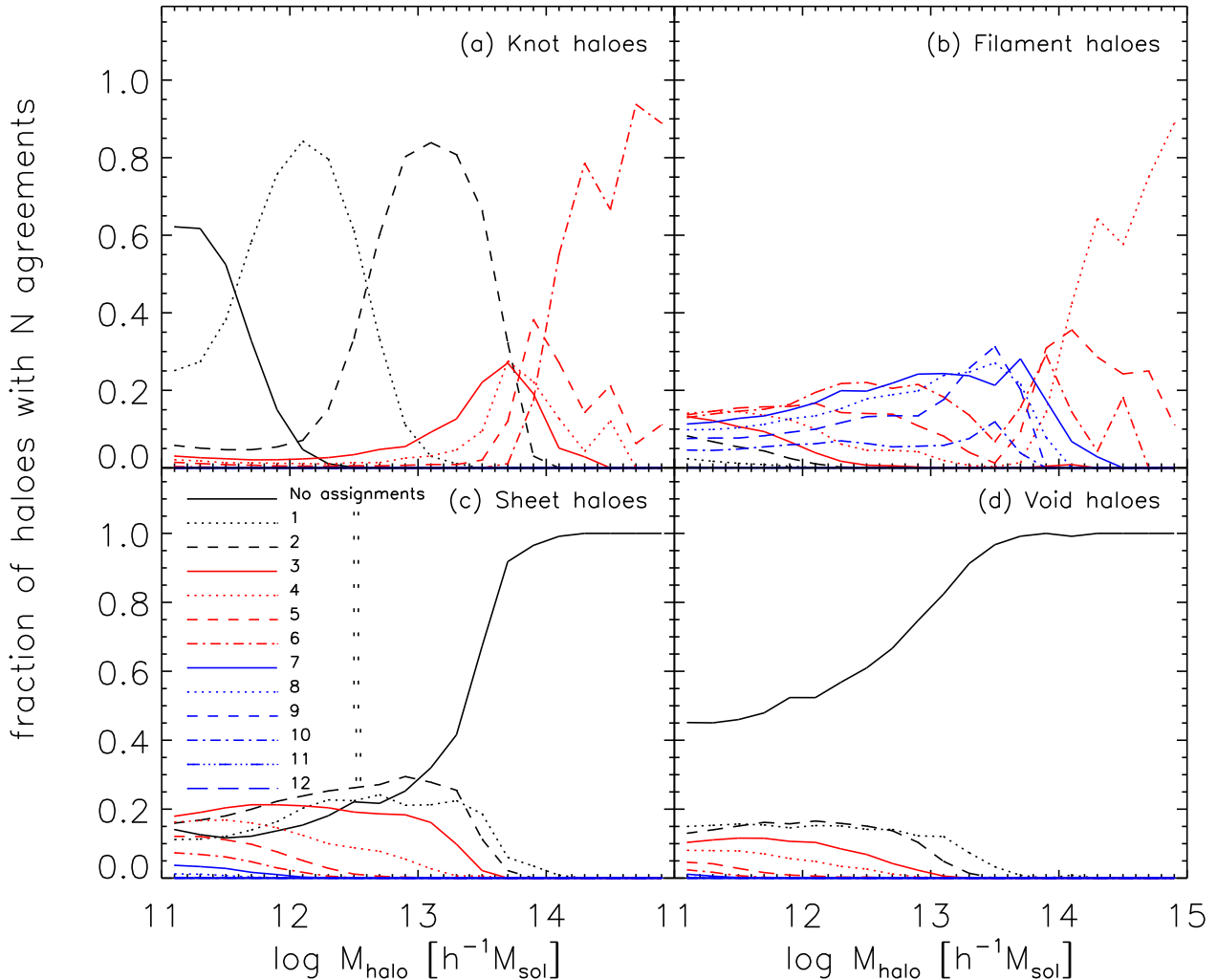
Figure 7. The level of agreement, on a halo by halo basis, in assigning a web classification to a given halo. For each halo in a given mass bin, we ask how many methods have assigned it the same web type. We plot the fraction of these haloes as a function of halo mass for the four web environments: knots (top-left), filaments (top-right), sheets (bottom-left) and voids (bottom-right). Each line shows the fraction of haloes at fixed halo mass that were assigned by N methods to that environment, with N from 0 (no assignments) to 10 (all methods agree). Note that not all methods identify all web types, so that the maximum number of agreements varies with web type: 6 for knots, 12 for filaments, 9 for sheets and 10 for voids.

exactly how much this is, with methods predicting either $\sim$15 per cent (V-web, CLASSIC), $\sim$5 per cent (T-web, DisPerSE) or $\lesssim$1 per cent (NEXUS+, ORIGAMI, MSWA, Spineweb, MMF-2) of halo mass in voids.

It is important to compare the environment tag associated with haloes on a halo per halo basis too, not only globally as is the case when comparing halo mass functions. To accomplish this, we ask the following question: for haloes in a given mass range, how many methods agree that some fraction of these have the same cosmic-web environment? The answer to this question is shown in Fig. 7.

To better understand our analysis, let us consider the panel of Fig. 7(a), which gives the agreement across methods for individual knot haloes. For high halo masses, $M \gtrsim 10^{14}\, h^{-1}\, \mathrm{M_{\odot}}$, the panel shows that most such haloes ($\sim$90 per cent) are assigned to knots by all the six methods (namely: NEXUS+, T-web, V-web, CLASSIC, ORIGAMI and MSWA) that identify knot environments (dot–dashed red curve). Conversely, 60 per cent of the smallest haloes (with $M \sim 10^{11}\, h^{-1}\, \mathrm{M_{\odot}}$) are not assigned by any method to the knot environment (solid black curve). In between the two extreme masses, we find two bell-like curves where haloes with $M \sim 10^{12}\, h^{-1}\, \mathrm{M_{\odot}}$ are assigned to knots by only one method

(black dotted curve), and haloes with $M \sim 10^{13}\, h^{-1}\, \mathrm{M_{\odot}}$ (black dashed curve) are assigned to knots by the two phase-space methods, MSWA and ORIGAMI.

In Fig. 7(b), we show the agreement among filament haloes. Note the two peaks in the blue dashed and blue dot–dashed lines at $M_{\mathrm{halo}} \approx 10^{13.5}$: nine methods agree that $\sim$30 per cent of haloes of this mass are in filaments while 10 methods agree that at least 10 per cent of haloes of this mass are in filaments. Here, four methods (DisPerSE, Spineweb, MMF-2 and MST) place the most massive haloes in filaments. Figs 7(c) and 7(d) indicate that no method puts the most massive haloes in sheets or voids. Specifically, this means that no haloes with $M \gtrsim 10^{14}\, h^{-1}\, \mathrm{M_{\odot}}$ are found in sheets, and no haloes with $M \gtrsim 10^{13.5}\, h^{-1}\, \mathrm{M_{\odot}}$ are found in voids, by any method.

The degree of agreement of web classifiers on a halo per halo basis varies accordingly to the spatial distribution of haloes, as we illustrate in Fig. 8. Here, each halo is coloured by how many methods agree on its given classification. Because the number of methods capable of assigning haloes to a given web type changes (e.g. filament-only finders cannot identify knot haloes, etc.) the colour scheme is not identical in each panel (see caption for exact colour explanation). In general, if many of the capable methods
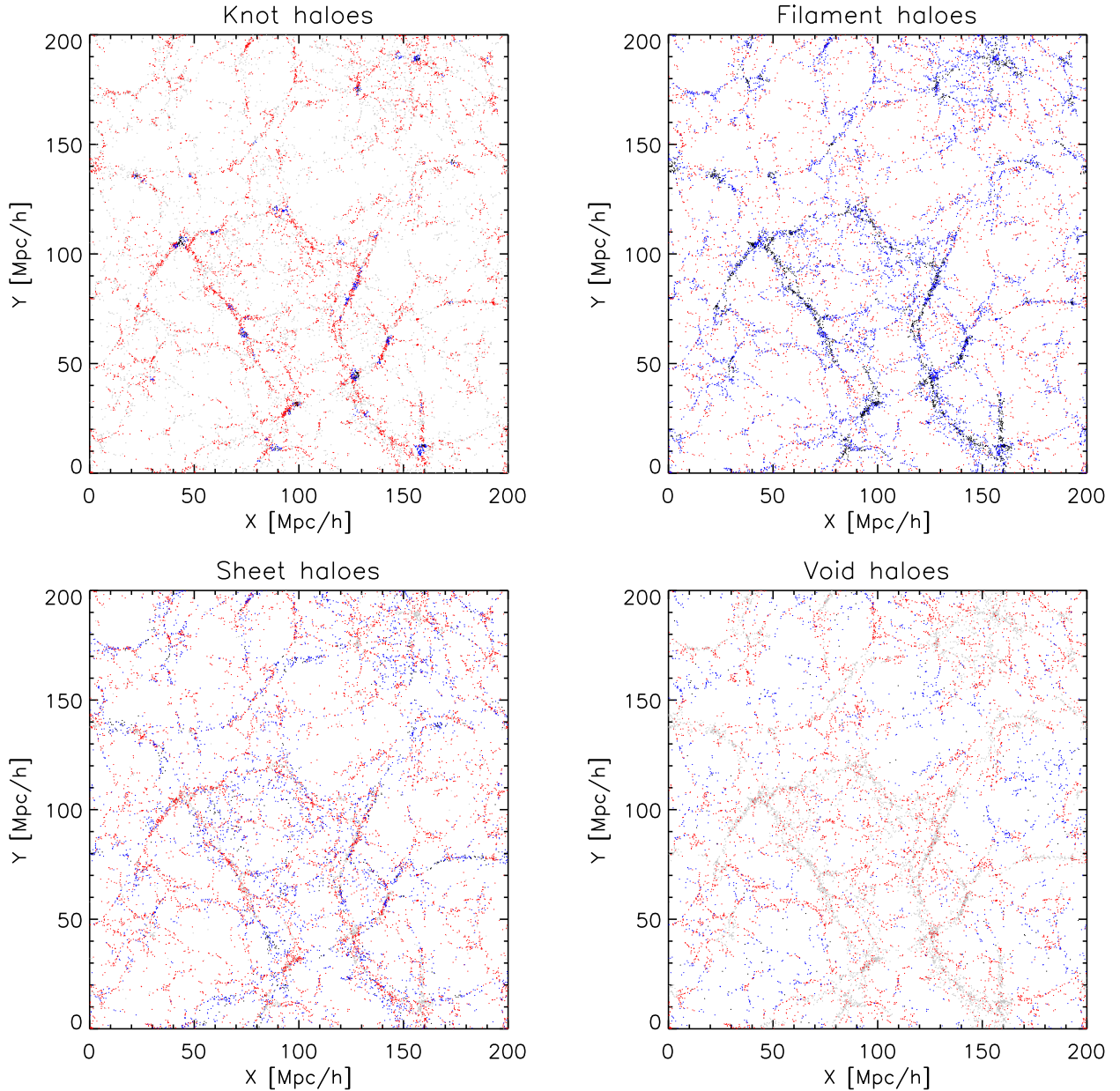
Figure 8. A visualization of the agreement across methods regarding a specific halo's classification shown in the same $10\,h^{-1}$ Mpc thick slice as in Figs 1–3. Not all web types are identified by each method, so for each panel the various colours indicate a different number of agreements. In the 'Knot haloes' panel, a halo is plotted in black if 5–6 methods agree, blue if 3–4 methods agree and red if 1–2 methods agree that a halo is in a knot. In the 'Filament haloes' panel colours represent: black if 9–12 methods agree, blue if 4–8 methods agree and red if 1–3 methods agree that a halo is in a filament. For 'Sheet haloes' the colours represent: black if 7–9 methods agree, blue if 4–6 methods agree and red if 1–3 methods agree that a halo is in a sheet. For the 'Void haloes' the colours represent: black if 7–10 methods agree, blue if 4–6 methods agree and red if 1–3 methods agree that a halo is in a void. In all panels, haloes not assigned that web classification are shown in grey.

agree on a specific halo's classification the halo is shown in black; if around half of the capable methods agree, the halo is plotted in blue. If a small number of capable methods agree, the halo is plotted in red. If no method assigns a halo a given classification, the halo is plotted in grey.

Fig. 8 'Knot' and 'Filament' halo panels show quite clearly that the haloes where the most methods agree belong to a biased set and are not simply random. Knot haloes find the most agreement in the densest areas of the simulation – a reassuring result. Similarly, those haloes that by eye appear to define the filamentary network too have the most agreements. Accordingly, none of the haloes in either the densest parts of the simulation or in the filaments are assigned

as void haloes (appearing as grey points). Sheets appear, as often is the case, as tenuous structures. Fig. 8 indicates that most or many methods are likely to agree on a specific halo's classification based on its location.

6 SUMMARY AND CONCLUSIONS

Large galaxy redshift surveys (e.g. 2dFGRS, SDSS, 2MRS) reveal that at megaparsec scales the Universe has a salient web-like structure. On these scales, the galaxies and the matter distribution in the universe has arranged itself into a complex web-like network of dense, interconnected knots, elongated filaments,

2D sheets and large nearly empty voids. These cosmic environments characterize the universe on the largest scales. One important aspect of the cosmic web is its multiscale character, manifesting itself in the existence of web-like structures over a sizeable range of scale. High-resolution simulations have revealed that such structures can be found down to very small scales, even down to the virial radius of haloes, and that they play a prominent role in the accretion of cold gas on to young and assembling protogalaxies in the early Universe (Danovich et al. 2012). It ties in with the results of a range of recent studies that have analysed the role of environment on the formation and the evolution of galaxies (e.g. Carollo et al. 2013; Creasey et al. 2015; Eardley et al. 2015; Guo, Tempel & Libeskind 2015; Martínez, Muriel & Coenda 2016; Poudel et al. 2017). Furthermore, theoretical studies have suggested that around half of the warm gas in the Universe is hiding in a 'warm-hot intergalactic medium', presumably in the filaments of the cosmic web (e.g. Eckert et al. 2015). It has therefore become of key importance to gain more insight into the structure and dynamics of the web-like universe, and into the interaction of the cosmic web with galaxy scale processes.

The cosmic web is one of the most intriguing and striking patterns found in nature, rendering its analysis and characterization far from trivial. This is evidenced by the many elaborate descriptions that have been developed. The absence of an objective and quantitative procedure for identifying and isolating knots, filaments, sheets and voids in the cosmic matter distribution has been a major obstacle in investigating the structure and dynamics of the cosmic web. The overwhelming complexity of the individual structures and their connectivity, the huge range of densities and the intrinsic multiscale nature prevent the use of simple tools. Over the past years, we have seen the introduction and proliferation of many new approaches and techniques. These methods are very varied in how they identify the cosmic-web environments; being designed with different cosmological data in mind and to answer different questions. These issues are compounded since the techniques available to theorists and simulators differ substantially from those employed by observers. This makes it even more important to understand how the various web identification methods compare with each other.

The main driver of this paper is to quantify in a systematic way both the similarities and differences between cosmic-web finders. There is no well-motivated common framework to objectively define the constituents of the cosmic web, so there is no way of judging which methods are successful or which ones are – in some objective way – 'better'. As such, the goal is to compare the output of the various methods to better relate studies that use different web identification methods. We proceeded by comparing several basic properties of the cosmic web: the mass and VFF of each component, the density distribution and the halo mass function in each environment, and a halo by halo comparison of their environment tag. For this, we asked the authors of each method to apply their technique to the same data, the output of an *N*-body simulation, and to return the resulting web classification in a common format.

We find a substantial diversity in the properties of the cosmic web across the various methods. This is to be expected given the challenges inherent in identifying the cosmic web and the multitude of approaches undertaken in doing so. In spite of this, we also find many similarities across the methods. Some of the most important agreements are as follows:

(i) Voids correspond to the most underdense regions and are consistently identified as such by all the methods. The voids occupy the largest volume fraction, with the majority of methods finding a ∼70 per cent VFF.

(ii) Most methods, except ORIGAMI and T-web, find that knots contain ∼10 per cent of the total mass in less than 1 per cent of the volume of the universe.

(iii) All the methods find that the density PDF systematically shifts towards lower densities as we go from knots to filaments, than to sheets and voids. Despite this trend, there is still a substantial overlap between the density PDF of different environments, which suggests that a simple density is inadequate for cosmic-web identification.

(iv) Most massive haloes, $M \gtrsim 10^{14} \, h^{-1} \, \mathrm{M}_{\odot}$, are classified as residing in knot environments by all the methods that identify knots.

(v) The voids are only sparsely populated with haloes and they lack completely massive haloes with $M \gtrsim 10^{13.5} \, h^{-1} \, \mathrm{M}_{\odot}$.

We have a very incomplete knowledge of what is the effect of environment on galaxy formation and evolution or of what is the cosmological information encoded in the cosmic-web pattern. The lack of knowledge is a result of the limitations of analytical approaches in modelling these non-linear processes. Each web finder captures different aspects of this very complex pattern, i.e. the cosmic web, so it is a worthwhile pursuit to analyse the connection between the environments identified by each method and the effect on galaxies and cosmological constraints.

REFERENCES

Abel T., Hahn O., Kaehler R., 2012, MNRAS, 427, 61
Adler R. J., 1981, The Geometry of Random Fields. Wiley, New York
Alpaslan M. et al., 2014a, MNRAS, 438, 177

Alpaslan M. et al., 2014b, MNRAS, 440, L106

Alpaslan M. et al., 2015, MNRAS, 451, 3249

Alpaslan M. et al., 2016, MNRAS, 457, 2287

Aragon-Calvo M. A., Szalay A. S., 2013, MNRAS, 428, 3409

Aragón-Calvo M. A., Yang L. F., 2014, MNRAS, 440, L46

Aragón-Calvo M. A., Jones B. J. T., van de Weygaert R., van der Hulst J. M., 2007a, A&A, 474, 315

Aragón-Calvo M. A., van de Weygaert R., Jones B. J. T., van der Hulst J. M., 2007b, ApJ, 655, L5

Aragón-Calvo M. A., van de Weygaert R., Araya-Melo P. A., Platen E., Szalay A. S., 2010a, MNRAS, 404, L89

Aragón-Calvo M. A., van de Weygaert R., Jones B. J. T., 2010b, MNRAS, 408, 2163

Aragón-Calvo M. A., Platen E., van de Weygaert R., Szalay A. S., 2010c, ApJ, 723, 364

Aragón-Calvo M. A., Neyrinck M. C., Silk J., 2016, preprint (arXiv:1607.07881)

Bardeen J. M., Bond J. R., Kaiser N., Szalay A. S., 1986, ApJ, 304, 15

Barrow J., Bhavsar S., Sonoda D., 1985, MNRAS, 216, 17

Bharadwaj S., Bhavsar S. P., Sheth J. V., 2004, ApJ, 606, 25

Bond J., Myers S., 1996, ApJS, 103, 1

Bond J. R., Kofman L., Pogosyan D., 1996, Nature, 380, 603

Bond N. A., Strauss M. A., Cen R., 2010a, MNRAS, 406, 1609

Bond N. A., Strauss M. A., Cen R., 2010b, MNRAS, 409, 156

Bos E. G. P., van de Weygaert R., Dolag K., Pettorino V., 2012, MNRAS, 426, 440

Carlesi E. et al., 2016, MNRAS, 458, 900

Carollo C. M. et al., 2013, ApJ, 776, 71

Cautun M. C., van de Weygaert R., 2011, Astrophysics Source Code Library, record ascl:1105.003

Cautun M., van de Weygaert R., Jones B. J. T., 2013, MNRAS, 429, 1286

Cautun M., van de Weygaert R., Jones B. J. T., Frenk C. S., 2014, MNRAS, 441, 2923

Cautun M., Bose S., Frenk C. S., Guo Q., Han J., Hellwing W. A., Sawala T., Wang W., 2015, MNRAS, 452, 3838

Chazal F., Cohen-Steiner D., Mérigot Q., 2009, INRIA Rapport de Récherche 6930

Chincarini G., Rood H. J., 1975, Nature, 257, 294

Choi E., Bond N. A., Strauss M. A., Coil A. L., Davis M., Willmer C. N. A., 2010, MNRAS, 406, 320

Codis S., Pichon C., Devriendt J., Slyz A., Pogosyan D., Dubois Y., Sousbie T., 2012, MNRAS, 427, 3320

Colberg J., 2007, MNRAS, 375, 337

Colberg J. M., Krughoff K. S., Connolly A. J., 2005, MNRAS, 359, 272

Colberg J. M. et al., 2008, MNRAS, 387, 933

Colless M. et al., 2003, preprint (astro-ph/0306581)

Colombi S., Pogosyan D., Souradeep T., 2000, Phys. Rev. Lett., 85, 5515

Courtois H. M., Pomarède D., Tully R. B., Hoffman Y., Courtois D., 2013, AJ, 146, 69

Creasey P., Scannapieco C., Nuza S. E., Yepes G., Gottlöber S., Steinmetz M., 2015, ApJ, 800, L4

de Lapparent V., Geller M., Huchra J., 1986, ApJ, 302, L1

de Vaucouleurs G., 1953, AJ, 58, 30

Danovich M., Dekel A., Hahn O., Teyssier R., 2012, MNRAS, 422, 1732

Danovich M., Dekel A., Hahn O., Ceverino D., Primack J., 2015, MNRAS, 449, 2087

Davis M., Efstathiou G., Frenk C. S., White S. D. M., 1985, ApJ, 292, 371

Dekel A. et al., 2009a, Nature, 457, 451

Dekel A., Sari R., Ceverino D., 2009b, ApJ, 703, 785

Doroshkevich A. G., 1970, Astrophysics, 6, 320

Doroshkevich A., Tucker D. L., Allam S., Way M. J., 2004, A&A, 418, 7

Dressler A., 1980, ApJ, 236, 351

Dubois Y. et al., 2014, MNRAS, 444, 1453

Eardley E. et al., 2015, MNRAS, 448, 3665

Eckert D. et al., 2015, Nature, 528, 105

Edelsbrunner H., Harer J., 2010, Computational Topology: An Introduction. Applied mathematics, American Mathematical Society, Available at: http://books.google.at/books?id=MDXa6gFRZuIC

Edelsbrunner H., Letscher J., Zomorodian A., 2002, Discrete Comput. Geom., 28, 511

Einasto J. et al., 2011, A&A, 534, A128

Fairall A. P., ed., 1998, Large-Scale Structures in the Universe

Falck B., Neyrinck M. C., 2015, MNRAS, 450, 3239

Falck B. L., Neyrinck M. C., Szalay A. S., 2012, ApJ, 754, 126

Falck B., Koyama K., Zhao G.-b., Li B., 2014, J. Cosmology Astropart. Phys., 7, 058

Florack L. M. J., Romeny B. M. T. H., Koenderink J. J., Viergever M. A., 1992, Image Vis. Comput., 10, 376

Forero-Romero J. E., González R., 2015, ApJ, 799, 45

Forero-Romero J. E., Hoffman Y., Gottlöber S., Klypin A., Yepes G., 2009, MNRAS, 396, 1815

Forman R., 1998, Adv. Math., 134, 90

Frenk C. S. et al., 1999, ApJ, 525, 554

Geller M. J., Huchra J. P., 1989, Science, 246, 897

Genovese C. R., Perone-Pacifico M., Verdinelli I., Wasserman L., 2010, preprint (arXiv:1003.5536)

Gillet N., Ocvirk P., Aubert D., Knebe A., Libeskind N., Yepes G., Gottlöber S., Hoffman Y., 2015, ApJ, 800, 34

Giovanelli R., Haynes M. P., 1985, AJ, 90, 2445

Goerdt T., Ceverino D., Dekel A., Teyssier R., 2015, MNRAS, 454, 637

González R. E., Padilla N. D., 2010, MNRAS, 407, 1449

González R. E., Padilla N. D., 2016, ApJ, 829, 58

González R. E., Prieto J., Padilla N., Jimenez R., 2017, MNRAS, 464, 4666

Gott III J. R., Jurić M., Schlegel D., Hoyle F., Vogeley M., Tegmark M., Bahcall N., Brinkmann J., 2005, ApJ, 624, 463

Graham M., Clowes R., 1995, MNRAS, 275, 790

Gregory S. A., Thompson L. A., Tifft W. G., 1978, BAAS, 10, 622

Guo Q., Tempel E., Libeskind N. I., 2015, ApJ, 800, 112

Gurbatov S. N., Saichev A. I., Shandarin S. F., 1989, MNRAS, 236, 385

Guzzo L. et al., 2014, A&A, 566, A108

Gyulassy A. G., 2008, PhD thesis, UC Davis

Hahn O., 2009, PhD thesis, ETH Zürich

Hahn O., Porciani C., Carollo C. M., Dekel A., 2007a, MNRAS, 375, 489

Hahn O., Carollo C. M., Porciani C., Dekel A., 2007b, MNRAS, 381, 41

Heinrich P., Stoica R. S., Tran V. C., 2012, Spat. Stat., 2, 47

Heß S., Kitaura F.-S., Gottlöber S., 2013, MNRAS, 435, 2065

Hidding J., 2017, PhD thesis, Univ. Groningen

Hidding J., van de Weygaert R., Vegter G., Jones B. J. T., Teillaud M., 2012, preprint (arXiv:1205.1669)

Hidding J., Shandarin S. F., van de Weygaert R., 2014, MNRAS, 437, 3442

Hirv A., Pelt J., Saar E., Tago E., Tamm A., Tempel E., Einasto M., 2017, A&A, 599, A31

Hoffman Y., Metuki O., Yepes G., Gottlöber S., Forero-Romero J. E., Libeskind N. I., Knebe A., 2012, MNRAS, 425, 2049

Hoffman Y., Pomarède D., Tully R. B., Courtois H. M., 2017, Nat. Astron., 1, 0036

Hoyle F., 1951, in Problems of Cosmical Aerodynamics. p. 195

Huchra J. P. et al., 2012, ApJS, 199, 26

Ibata R. A. et al., 2013, Nature, 493, 62

Icke V., 1973, A&A, 27, 1

Icke V., 1984, MNRAS, 206, 1P

Jõeveer M., Einasto J., Tago E., 1978, MNRAS, 185, 357

Jones B. J. T., van de Weygaert R., Aragón-Calvo M. A., 2010, MNRAS, 408, 897

Kirshner R. P., Oemler A. J., Schechter P. L., Shectman S. A., 1981, ApJ, 248, L57

Kirshner R. P., Oemler A., Jr, Schechter P. L., Shectman S. A., 1987, ApJ, 314, 493

Kitaura F.-S., 2013, MNRAS, 429, L84

Kitaura F.-S., Angulo R. E., 2012, MNRAS, 425, 2443

Knebe A., Gill S. P. D., Gibson B. K., Lewis G. F., Ibata R. A., Dopita M. A., 2004, ApJ, 603, 7

Knebe A. et al., 2011, MNRAS, 415, 2293

Knebe A. et al., 2013, MNRAS, 435, 1618

Kofman L., Pogosian D., Shandarin S., 1990, MNRAS, 242, 200

Kofman L., Pogosyan D., Shandarin S. F., Melott A. L., 1992, ApJ, 393, 437

Kraan-Korteweg R. C., Cluver M. E., Bilicki M., Jarrett T. H., Colless M., Elagali A., Böhringer H., Chon G., 2017, MNRAS, 466, L29

Kuutma T., Tamm A., Tempel E., 2017, A&A, 600, L6

Lahav O., Santiago B. X., Webster A. M., Strauss M. A., Davis M., Dressler A., Huchra J. P., 2000, MNRAS, 312, 166

Lavaux G., Wandelt B. D., 2010, MNRAS, 403, 1392

Lavaux G., Wandelt B. D., 2012, ApJ, 754, 109

Leclercq F., Jasche J., Sutter P. M., Hamaus N., Wandelt B., 2015a, J. Cosmology Astropart. Phys., 3, 047

Leclercq F., Jasche J., Wandelt B., 2015b, J. Cosmology Astropart. Phys., 6, 015

Leclercq F., Jasche J., Wandelt B., 2015c, A&A, 576, L17

Leclercq F., Jasche J., Lavaux G., Wandelt B., Percival W., 2017, J. Cosmology Astropart. Phys., 6, 049

Leclercq F., Lavaux G., Jasche J., Wandelt B., 2016, J. Cosmology Astropart. Phys., 8, 027

Lee J., Park D., 2009, ApJ, 696, L10

Lee J., Pen U.-L., 2000, ApJ, 532, L5

Li Q., Sone S., Doi K., 2003, Med. Phys., 30, 2040

Libeskind N. I., Hoffman Y., Knebe A., Steinmetz M., Gottlöber S., Metuki O., Yepes G., 2012, MNRAS, 421, L137

Libeskind N. I., Hoffman Y., Forero-Romero J., Gottlöber S., Knebe A., Steinmetz M., Klypin A., 2013a, MNRAS, 428, 2489

Libeskind N. I., Hoffman Y., Steinmetz M., Gottlöber S., Knebe A., Hess S., 2013b, ApJ, 766, L15

Libeskind N. I., Hoffman Y., Gottlöber S., 2014a, MNRAS, 441, 1974

Libeskind N. I., Knebe A., Hoffman Y., Gottlöber S., 2014b, MNRAS, 443, 1274

Libeskind N. I., Hoffman Y., Tully R. B., Courtois H. M., Pomarède D., Gottlöber S., Steinmetz M., 2015a, MNRAS, 452, 1052

Libeskind N. I., Tempel E., Hoffman Y., Tully R. B., Courtois H., 2015b, MNRAS, 453, L108

Lietzen H. et al., 2016, A&A, 588, L4

Lindeberg T., 1998, Int. J. Comput. Vis., 30, 79

Lynden-Bell D., Faber S. M., Burstein D., Davies R. L., Dressler A., Terlevich R. J., Wegner G., 1988, ApJ, 326, 19

Martínez H. J., Muriel H., Coenda V., 2016, MNRAS, 455, 127

Metuki O., Libeskind N. I., Hoffman Y., Crain R. A., Theuns T., 2015, MNRAS, 446, 1458

Metuki O., Libeskind N. I., Hoffman Y., 2016, MNRAS, 460, 297

Milnor J., 1963, J. Math. Phys.

Morse M., 1934, Am. Math. Soc. Colloquium Publ., 18, 1

Murphy D. N. A., Eke V. R., Frenk C. S., 2011, MNRAS, 413, 2288

Nevalainen J. et al., 2015, A&A, 583, A142

Neyrinck M. C., 2008, MNRAS, 386, 2101

Neyrinck M. C., 2012, MNRAS, 427, 494

Novikov D., Colombi S., Doré O., 2006, MNRAS, 366, 1201

Nuza S. E., Kitaura F.-S., Heß S., Libeskind N. I., Müller V., 2014, MNRAS, 445, 988

Okabe A., Boots B., Sugihara K., Chiu S. N., 2000, Spatial tessellations: Concepts and applications of Voronoi diagrams, 2nd edn. Wiley, New York

Pahwa I. et al., 2016, MNRAS, 457, 695

Pan D. C., Vogeley M. S., Hoyle F., Choi Y.-Y., Park C., 2012, MNRAS, 421, 926

Park D., Lee J., 2007, Phys. Rev. Lett., 98, 081301

Peebles P. J. E., 1969, ApJ, 155, 393

Peebles P. J. E., 1980, The Large Scale Structure of the Universe, Princeton Univ. Press, Princeton, NJ

Pichon C., Codis S., Pogosyan D., Dubois Y., Desjacques V., Devriendt J., 2016, in van de Weygaert R., Shandarin S., Saar E., Einasto J., eds, Proc. IAU Symp. 308, The Zeldovich Universe: Genesis and Growth of the Cosmic Web. Cambridge Univ. Press, Cambridge, p. 421

Pisani A., Sutter P. M., Hamaus N., Alizadeh E., Biswas R., Wandelt B. D., Hirata C. M., 2015, Phys. Rev. D, 92, 083531

Planck Collaboration XVI, 2014, A&A, 571, A16

Platen E., van de Weygaert R., Jones B. J. T., 2007, MNRAS, 380, 551

Platen E., van de Weygaert R., Jones B. J. T., 2008, MNRAS, 387, 128

Pomarède D., Tully R. B., Hoffman Y., Courtois H. M., 2015, ApJ, 812, 17

Poudel A., Heinämäki P., Tempel E., Einasto M., Lietzen H., Nurmi P., 2017, A&A, 597, A86

Proust D. et al., 2006, A&A, 447, 133

Ramachandra N. S., Shandarin S. F., 2015, MNRAS, 452, 1643

Ramachandra N. S., Shandarin S. F., 2017, MNRAS, 467, 1748

Romano-Díaz E., van de Weygaert R., 2007, MNRAS, 382, 2

Sahni V., Coles P., 1995, Phys. Rep., 262, 1

Sahni V., Sathyaprakah B. S., Shandarin S. F., 1994, ApJ, 431, 20

Sato Y., Nakajima S., Shiraga N., Atsumi H., Yoshida S., Koller T., Gerig G., Kikinis R., 1998, Med. Image Anal., 2, 143

Scannapieco C. et al., 2012, MNRAS, 423, 1726

Schaap W. E., van de Weygaert R., 2000, A&A, 363, L29

Schaye J. et al., 2015, MNRAS, 446, 521

Shandarin S. F., 2011, J. Cosmology Astropart. Phys., 5, 15

Shandarin S. F., Sunyaev R., 2009, A&A, 500, 19

Shandarin S., Zel'dovich Y., 1989, Rev. Mod. Phys., 61, 185

Shandarin S. F., Sheth J. V., Sahni V., 2004, MNRAS, 353, 162

Shandarin S., Habib S., Heitmann K., 2012, Phys. Rev. D, 85, 083005

Shapley H., 1930, Harv. Coll. Obs. Bull., 874, 9

Shectman S. A., Landy S. D., Oemler A., Tucker D. L., Lin H., Kirshner R. P., Schechter P. L., 1996, ApJ, 470, 172

Shen J., Abel T., Mo H. J., Sheth R. K., 2006, ApJ, 645, 783

Sheth R. K., Tormen G., 1999, MNRAS, 308, 119

Sheth R., van de Weygaert R., 2004, MNRAS, 350, 517

Shivashankar N., Pranav P., Natarajan V., van de Weygaert R., Bos E. P., Rieder S., 2016, IEEE Trans. Vis. Comput. Graphics, 22, 1745

Sorce J. G. et al., 2016, MNRAS, 455, 2078

Sousbie T., 2011, MNRAS, 414, 350

Sousbie T., Pichon C., Colombi S., Novikov D., Pogosyan D., 2008a, MNRAS, 383, 1655

Sousbie T., Pichon C., Courtois H., Colombi S., Novikov D., 2008b, ApJ, 672, L1

Sousbie T., Colombi S., Pichon C., 2009, MNRAS, 393, 457

Sousbie T., Pichon C., Kawahara H., 2011, MNRAS, 414, 384

Springel V., 2005, MNRAS, 364, 1105

Springel V. et al., 2005, Nature, 435, 629

Stoica R. S., Gregori P., Mateu J., 2005, Stoch. Process. Appl., 115, 1860

Stoica R. S., Martínez V. J., Saar E., 2007, J. R. Stat. Soc. C, 56, 459

Stoica R. S., Martínez V. J., Saar E., 2010, A&A, 510, A38

Sutter P. M., Lavaux G., Wandelt B. D., Weinberg D. H., 2012, ApJ, 761, 44

Sutter P. M., Carlesi E., Wandelt B. D., Knebe A., 2015, MNRAS, 446, L1

Tegmark M. et al., 2004, ApJ, 606, 702

Tempel E., Libeskind N. I., 2013, ApJ, 775, L42

Tempel E., Tamm A., 2015, A&A, 576, L5

Tempel E., Stoica R. S., Saar E., 2013, MNRAS, 428, 1827

Tempel E., Stoica R. S., Martínez V. J., Liivamägi L. J., Castellan G., Saar E., 2014, MNRAS, 438, 3465

Tempel E., Guo Q., Kipper R., Libeskind N. I., 2015, MNRAS, 450, 2727

Tempel E., Stoica R. S., Kipper R., Saar E., 2016, Astron. Comput., 16, 17

Trowland H. E., 2013, PhD thesis, Univ. Sydney

Trowland H. E., Lewis G. F., Bland-Hawthorn J., 2013, ApJ, 762, 72

Tully R. B., Fisher J. R., 1987, Atlas of Nearby Galaxies

Tully R. B., Shaya E. J., Karachentsev I. D., Courtois H. M., Kocevski D. D., Rizzi L., Peel A., 2008, ApJ, 676, 184

Tully R. B., Courtois H., Hoffman Y., Pomarède D., 2014, Nature, 513, 71

van de Weygaert R., 1994, A&A, 283, 361

van de Weygaert R., 2016, in van de Weygaert R., Shandarin S., Saar E., Einasto J., eds, Proc. IAU Symp. 308, The Zeldovich Universe: Genesis and Growth of the Cosmic Web. Cambridge Univ. Press, Cambridge, p. 493

van de Weygaert R., Bertschinger E., 1996, MNRAS, 281, 84

van de Weygaert R., Bond J. R., 2008, in Plionis M., López-Cruz O., Hughes
    D., eds, Lecture Notes in Physics, Vol. 740, A Pan-Chromatic View of
    Clusters of Galaxies and the Large-Scale Structure. Springer-Verlag,
    Berlin, p. 335

van de Weygaert R., Schaap W., 2009, in Martínez V. J., Saar E., Martínez-
    González E., Pons-Bordería M.-J., eds, Lecture Notes in Physics, Vol.
    665, Data Analysis in Cosmology. Springer-Verlag, Berlin, p. 291

van de Weygaert R., Shandarin S., Saar E., Einasto J., s, 2016, Proc. IAU
    Symp. 308, The Zeldovich Universe: Genesis and Growth of the Cosmic
    Web. Cambridge Univ. Press, Cambridge

van Haarlem M., van de Weygaert R., 1993, ApJ, 418, 544

Vogelsberger M. et al., 2014, MNRAS, 444, 1518

Wojtak R., Knebe A., Watson W. A., Iliev I. T., Heß S., Rapetti D., Yepes
    G., Gottlöber S., 2014, MNRAS, 438, 1805

Wu Y., Batuski D. J., Khalil A., 2009, ApJ, 707, 1160

Zel'dovich Y. B., 1970, A&A, 5, 84

Zel'dovich Y. B., 1974, Fizika Sz., 24, 304

Zeldovich I. B., Einasto J., Shandarin S. F., 1982, Nature, 300, 407

[1]*Leibniz-Institute für Astrophysik Potsdam (AIP), An der Sternwarte 16,
D-14482 Potsdam, Germany*

[2]*Kapteyn Astronomical Institute, University of Groningen, PO Box 800,
NL-9700 AV Groningen, the Netherlands*

[3]*Institute for Computational Cosmology, Durham University, South Road,
Durham, DH1 3LE, UK*

[4]*Institute of Theoretical Astrophysics, University of Oslo, PO Box 1029
Blindern, N-0315 Oslo, Norway*

[5]*Tartu Observatory, Observatooriumi 1, 61602 Tõravere, Estonia*

[6]*Kavli Institute for Particle Astrophysics and Cosmology, Stanford Univer-
sity, Menlo Park, CA 94025, USA*

[7]*Department of Physics, Stanford University, Stanford, CA 94305, USA*

[8]*NASA Ames Research Center N232, Moffett Field, Mountain View, CA
94035, USA*

[9]*Instituto Astronomico de Ensenada,UNAM, Mexico*

[10]*Departamento de Física, Universidad de los Andes, Cra. 1 No. 18A-10,
Edificio Ip, Bogotá, 111711, Colombia*

[11]*Instituto de Astrofísica, Pontificia Universidad Catolica de Chile, Santi-
ago, 8970117 Chile*

[12]*Centro de Astro-Ingeniería, Pontificia Universidad Catolica de Chile,
Santiago, 8970117 Chile*

[13]*Observatoire de la Cote d'Azur, Laboratoire Lagrange, Boulevard de
l'Observatoire, CS 34229, F-06304 NICE, France*

[14]*Institute of Cosmology and Gravitation, University of Portsmouth,
Portsmouth PO1 3FX, UK*

[15]*Janusz Gil Institute of Astronomy, University of Zielona Góra, ul. Szafrana
2, PL-65-516 Zielona Góra, Poland*

[16]*Racah Institute of Physics, Hebrew University of Jerusalem, Givat Ram,
Jerusalem 91904, Israel*

[17]*Instituto de Astrofisica de Canarias (IAC), C/Vía Láctea, s/n, E-38200 La
Laguna, Tenerife, Spain*

[18]*Departamento Astrofísica, Universidad de La Laguna (ULL), E-38206 La
Laguna, Tenerife, Spain*

[19]*Departamento de Física Teórica, Módulo 15, Facultad de Ciencias, Uni-
versidad Autónoma de Madrid, E-28049 Madrid, Spain*

[20]*Astro-UAM, UAM, Unidad Asociada CSIC*

[21]*Scuola Normale Superiore, Piazza dei Cavalieri 7, I-56126 Pisa, Italy*

[22]*Instituto de Astronomía y Física del Espacio (IAFE, CONICETUBA), CC
67, Suc. 28, 1428 Buenos Aires, Argentina*

[23]*Department of Physics and Astronomy, University of Kansas, Lawrence,
KS 66045, USA*

[24]*ICRAR, M468, University of Western Australia, Crawley, WA 6009,
Australia*

[25]*Institut Elie Cartan de Lorraine, Université de Lorraine, F-54506
Vandoeuvre-lés-Nancy Cedex, France*

[26]*Institut de Mécanique Céleste et Calcul des Ephémérides (IMCCE), Ob-
servatoire de Paris, F-75014 Paris, France*

[27]*Institut d'Astrophysique de Paris, CNRS UMR 7095 and UPMC, 98bis,
bd Arago, F-75014 Paris, France*

This paper has been typeset from a TEX/LATEX file prepared by the author.